J. Fluid Mech. (2008), *vol.* 598, *pp.* 141–175.
doi:10.1017/S0022112007009706 Printed in the United Kingdom

Investigation of three-dimensional structure of fine scales in a turbulent jet by using cinematographic stereoscopic particle image velocimetry

B. GANAPATHISUBRAMANI[1], K. LAKSHMINARASIMHAN[2]† AND N. T. CLEMENS[2]

[1]Department of Aeronautics, Imperial College London, Prince Consort Road, London, SW7 2AZ, UK

[2]Center for Aeromechanics Research, The University of Texas at Austin, 210 E. 24th Street, WRW220, Mail Code C0604, Austin, TX 78712, USA

(Received 5 September 2006 and in revised form 26 October 2007)

Cinematographic stereoscopic particle image velocimetry measurements were performed to resolve small and intermediate scales in the far field of an axisymmetric co-flowing jet. Measurements were performed in a plane normal to the axis of the jet and the time-resolved measurement was converted to quasi-instantaneous three-dimensional data by using Taylor's hypothesis. The quasi-instantaneous three-dimensional data enabled computation of all nine components of the velocity gradient tensor over a volume. The results based on statistical analysis of the data, including computation of joint p.d.f.s and conditional p.d.f.s of the principal strain rates, vorticity and dissipation, are all in agreement with previous numerical and experimental studies, which validates the quality of the quasi-instantaneous data. Instantaneous iso-surfaces of the principal intermediate strain rate (β) show that sheet-forming strain fields (i.e. $\beta > 0$) are themselves organized in the form of sheets, whereas line-forming strain fields ($\beta < 0$) are organized into smaller spotty structures (not lines). Iso-surfaces of swirling strength (a vortex identification parameter) in the volume reveal that, in agreement with direct numerical simulation results, the intense vortex structures are in the form of elongated 'worms' with characteristic diameter of approximately 10η and characteristic length of 60–100η. Iso-surfaces of intense dissipation show that the most dissipative structures are in the form of sheets and are associated with clusters of vortex tubes. Approximately half of the total dissipation occurs in structures that are generally sheet-like, whereas the other half occurs in broad indistinct structures. The largest length scale of dissipation sheets is of order 60η and the characteristic thickness (in a plane normal to the axis of the sheet) is about 10η. The range of scales between 10η (thickness of dissipation sheets, diameter of vortex tubes) to 60η (size of dissipation sheet or length of vortex tubes) is consistent with the bounds for the dissipation range in the energy and dissipation spectrum as inferred from the three-dimensional model energy spectrum.

† Present address: GE Global Research, Bangalore, India.

1. Introduction

The structure of intermediate and fine scales in turbulent shear flows is a long-standing research problem and remains one of the most challenging aspects of turbulent flows. The dynamics of intermediate and fine scales of turbulent shear flows are important to turbulence theory and to the development and validation of subgrid scale models used in large-eddy simulations of shear flows.

Batchelor & Townsend (1949) first reported the presence of intermittency in turbulence, where the small-scale turbulent motions exhibit intense variations. They performed hot-wire anemometry and calculated higher-order velocity derivatives, indicating that the small scales in a turbulent flow are sparsely distributed in space. Batchelor & Townsend (1949) stated that vorticity and other gradient quantities (including dissipation) are made 'spotty' in the early stages of the decay and by some intrinsic instability are kept 'spotty' throughout the decay.

After the first investigation by Batchelor & Townsend (1949), several experimental studies worked towards statistical characterization of the small-scale motions (for example see Kuo & Corrsin 1971; Saddoughi & Veeravalli 1994). Most of these studies computed various statistical estimates like scaling exponents of probability density distributions (p.d.f.s), structure functions, skewness and flatness for various quantities such as vorticity, circulation and dissipation. A review of the work on statistical analysis of intermediate and small scales in turbulence can be found in Monin & Yaglom (1975) and Sreenivasan & Antonia (1997).

Statistical analysis of small scales does not reveal the geometrical structure of vorticity or dissipation fields. However, several researchers, including Betchov (1956), Tennekes (1968) and Lundgren (1982), have proposed models for the geometric structure of small-scale turbulence. Betchov (1956) proposed a model in which the presence of two positive principal strains causes vorticity to take the form of sheets. Tennekes (1968) proposed an alternative picture where the small-scale structures can be modelled as vortex tubes with diameter η (where η is the Kolmogorov scale). Lundgren (1982) introduced the strained spiral vortex model, which he found reproduced the $k^{-5/3}$ energy spectrum.

Kuo & Corrsin (1971) performed hot-wire measurements to investigate the spatial intermittency of turbulent shear flows and found that the extent of a typical active region (which is defined as a region over which the instantaneous value of a velocity gradient is several times larger than its mean value) was large compared to the fine-scale structure itself. They concluded that active regions are more nearly rod-like in shape rather than spherical or in the form of sheets. Schwarz (1990) performed flow visualization measurements of grid turbulence and concluded that the structures of small scales are in the form of layered sheets. The author also stated that the structures were found to exhibit a spatial variation limited by the Kolmogorov length scale. Douady, Couder & Brachet (1991) also performed flow visualization using air bubbles and found that the intermittent vortex structures possess a 'filamentary shape', and that these structures appear to become stretched/sheared due to larger coherent regions.

A complete analysis of the three-dimensional structure of dissipation, vorticity and other gradient quantities in turbulent flows requires detailed simultaneous three-dimensional velocities and velocity gradient information. Such information has been derived mainly from Direct Numerical Simulations (DNS) of turbulence. Although previous experimental and analytical studies provide a range of geometric models for the fine-scale structures, DNS studies of isotropic turbulence appear to agree that intense regions of vorticity tend to form tubes, also called 'worms' (for example, Siggia

1981; Kerr 1985; Ashurst *et al.* 1987; Vincent & Meneguzzi 1991; Ruetsch & Maxey 1991; Jimenez *et al.* 1993). Some researchers investigated the relationship between vorticity and dissipation (Kerr 1985; Brachet 1991; Kida & Ohkitani 1992; Vincent & Meneguzzi 1994) by visualizing these quantities, obtained from DNS datasets, simultaneously. These studies concluded that intense dissipative structures are found in the vicinity of intense vortex cores (or 'worms'). However, the exact structure of intense dissipation is not clearly defined. Brachet (1991) indicated that the regions of intense enstrophy are spatially more concentrated than the energy dissipation. Other studies found that the shape of the kinetic energy dissipation field is more complicated since it contains sheet-, line- and blob-like structures (Siggia 1981; Kerr 1985; Yamamoto & Hosokawa 1988).

Most experimental studies in the literature rely on point measurements or flow visualization techniques to speculate on the three-dimensional structure of the flow field. Therefore those studies cannot provide insight into the instantaneous spatial structure of the finest scales. Tsurikov (2003) performed two-component particle image velocimetry measurements to resolve small and intermediate scales of the flow, and concluded that intense regions of kinetic energy dissipation possessed sheet-like structures. However, planar measurements cannot capture the complete spatial structure of the flow field. Recently, Mullin & Dahm (2006*a*) performed dual-plane stereoscopic experiments to study the fine and intermediate scales of a turbulent shear flow. The technique enables computation of all nine velocity gradients over a plane; however, the information is available only over a plane and therefore cannot completely describe the three-dimensional structure. Zeff *et al.* (2003) reconstructed a three-dimensional velocity field based on simultaneous high-speed particle image velocimetry (PIV) measurements in three different planes of a small cube. The authors found that dissipation and enstrophy are spatially and temporally separated and are largely intermittent. Su & Dahm (1996) performed scalar imaging velocimetry where the complete velocity gradient tensor of the flow field was obtained by inversion of the conserved scalar transport equation. The authors investigated three-dimensional flow fields of enstrophy and dissipation and concluded that both quantities are relatively 'spotty' with large values occurring very rarely. The field of view of the above-mentioned study was approximately $15\eta \times 15\eta$, and as a result they were unable to resolve the intermediate scales of the flow field.

In the present study, time-resolved stereoscopic particle image velocimetry is utilized to measure three components of velocity in a plane and Taylor's hypothesis is employed to reconstruct a quasi-instantaneous volume of data. Experiments were performed in the far field of an axisymmetric co-flowing jet where the Kolmogorov scale is sufficiently large that the dissipation scales can be resolved. The pseudo-three-dimensional data are used to compute the complete velocity gradient tensor along with the three components of vorticity and other derived quantities such as three-dimensional dissipation rates. The goal of this study is to experimentally investigate the three-dimensional intermediate- and fine-scale spatial structure of vorticity and dissipation.

2. Experiment facility and techniques

Experiments were performed in the far field of a mildly co-flowing axisymmetric turbulent air jet. The co-flow facility is 920 mm wide by 920 mm long by 1170 mm high, and was constructed of aluminium structural members and aluminium sheet for the walls. The axisymmetric turbulent jet exhausted into a co-flow of air. The jet

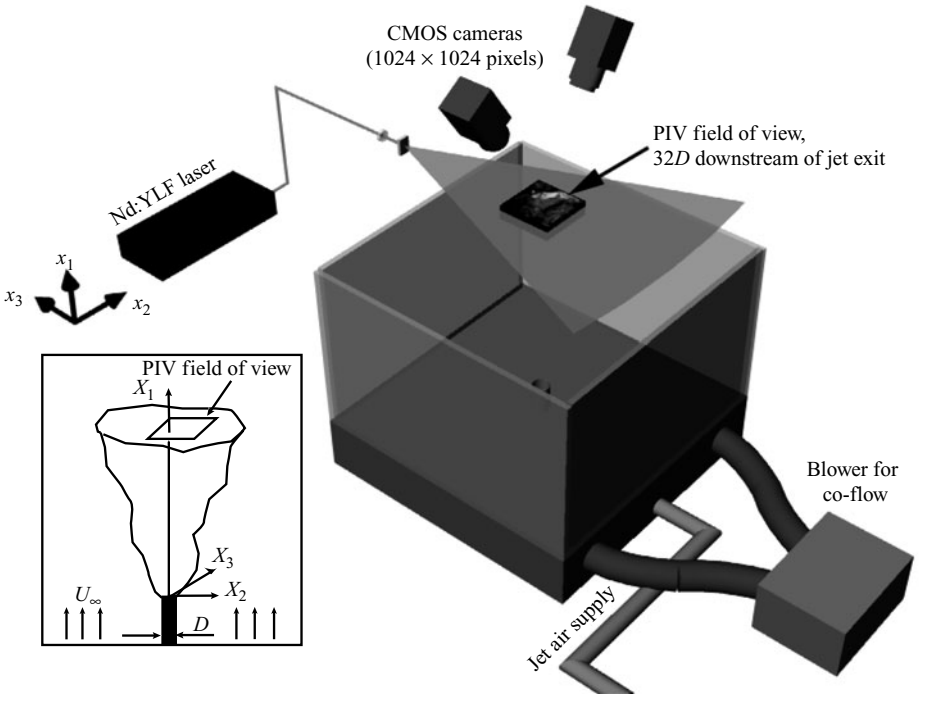

FIGURE 1. Schematic of the experimental setup. The inset shows a representative view of the co-flowing jet.

issued upwards from a circular pipe, 26 mm in diameter (D), located at the centre of the co-flow facility as shown in figure 1.

The jet fluid was air that was stored in a large high-pressure reservoir. The flow rate was controlled by a manually operated valve and monitored using an electronic mass flowmeter (McMillan 50D-15). Tsurikov (2003), who developed this experimental facility, obtained velocity profiles using hot-film probes and documented the presence of a fully developed turbulent pipe flow at the jet exit. The spectra at the centreline indicated a $-5/3$ spectrum and did not have any dominant frequency. He also performed additional hot-film and PIV measurements in various azimuthal planes to ensure that the jet was axisymmetric at the exit. The jet velocity at the exit was $U_o = 3\,\mathrm{m\,s^{-1}}$. The co-flow was supplied by an industrial blower (Grainger/Dayton model 5C508) which was operated at fixed speed. The co-flow entered the jet facility through a network of PVC pipes, and was conditioned by sections of honeycomb and fine-mesh screens prior to entering the test section. The co-flow velocity was $U_\infty = 0.15\,\mathrm{m\,s^{-1}}$. The boundary layer on the outside of the jet tube (due to the co-flow) was laminar with an estimated thickness of 11 mm near the jet exit. Additional details regarding design and construction of the flow facility and qualification of the flow field at the jet exit (i.e. axisymmetry of the jet, mean velocity profiles, turbulence intensities, etc.) are presented in Tsurikov (2003).

The following are some relevant length scales at the measurement location: jet half-width ($\delta_{1/2}$) = 126 mm, Taylor micro-scale (λ) = 13.8 mm and Kolmogorov scale (η) = 0.45 mm. The Kolmogorov scale ($\eta = (\nu^3/\bar{\epsilon})^{1/4}$, where ν is the kinematic viscosity and $\bar{\epsilon}$ is the mean dissipation rate) was initially computed using an estimate for the

mean dissipation that was based on local homogeneous isotropy. This calculation gave an estimate for $\eta = 0.53$ mm. However, as will be shown in the next section, the dissipation computed, based on the stereoscopic data, conformed to the dissipation estimate calculated, based on axisymmetric isotropy conditions prescribed by George & Hussein (1991). Therefore, the mean dissipation rate computed from the data was utilized to estimate the Kolmogorov scale quoted above ($\eta = 0.45$ mm). The Reynolds number based on jet exit velocity and diameter $Re_D = 5100$ and the Reynolds number based on Taylor micro-scale $Re_\lambda \approx 150$.

Cinematographic stereoscopic PIV measurements were performed in the 'end-view' plane (x_2–x_3) at a downstream axial location of $x_1 = 32D$. (In this study, x_1 is the axial direction, and x_2 and x_3 are the two orthogonal radial directions.) The cinematographic PIV system (shown in figure 1) consisted of an Nd:YLF laser (Coherent Evolution-90) with an output wavelength of 527 nm and a pair of high-framing rate 1024×1024 pixel resolution CMOS cameras (Photron FASTCAM-Ultima APX) that were operated at a rate of 2 kHz. Both cameras were fitted with a Nikon 105 mm lens with an aperture setting of f/5.6.

Glycerin-based droplets with a nominal size of 1–2 μm generated by a theatrical fog machine (Rosco Model 1600) were used as PIV seed particles. The response time (τ_R) of these seed particles is computed to be approximately 4 μs based on a particle diameter of 1 μm. The Stokes number, defined as $St = \tau_R/\tau_F$ (with τ_F the characteristic flow time scale) must be much less than 1 for the particles to faithfully track the fluid motion (Raffel, Willert & Kompenhans 1998). Given that the goal of this study is to track small-scale motions, the characteristic flow time is the Kolmogorov time scale $\tau_\eta = \sqrt{\nu/\epsilon}$, which is approximately 15 ms. This gives a Stokes number of 2.5×10^{-4} and hence indicates that the particles easily track the velocity fluctuations in the flow.

The particles were seeded into the co-flow and subsequently entrained by the developing jet. The seed particles were illuminated by a laser sheet (thickness $\approx$1 mm) and the scattered light was captured by the two CMOS cameras in stereoscopic arrangement. The cameras were oriented at an angle of 30° to the axis of the jet, as shown in figure 1, and the Scheimpflug condition was enforced to maintain focus across the entire field of view by orienting the lens plane at an angle to the image plane (the Scheimpflug condition ensures that particle images appear focused across the field of view: see Raffel *et al.* 1998 for details). This arrangement introduced a strong perspective distortion, and as a result the magnification varied across the image plane. This distortion was corrected by calibration using a fixed grid that contains marker points. The target was aligned with the laser sheet that illuminated the measurement plane, and the target subsequently translated at intervals of 0.5 mm in both directions normal to the laser sheet. Digital images of the grid were captured by both cameras for various locations of the target. The acquired images of the grid were analysed using TSI *PivCalib* software to compute the magnification at each axial location.

Cinematographic images were acquired for a duration of 1 s, corresponding to a total of 2000 frames and 2 GB of data for each experimental run. Images from the cameras were then transferred to a hard disk and processed to compute vector fields. Successive particle images in the movie sequence were correlated to compute PIV vector fields ($\Delta t = 500$ μs, since frequency of image acquisition is 2 kHz) with TSI *Insight 6.1* software. The final interrogation region was 16×16 pixels in size with 50% overlap. The vector fields were validated and the missing vectors were interpolated using a 3×3 local mean technique. The resulting vectors from each camera were then combined to compute all three velocity components. The resolution of the resulting

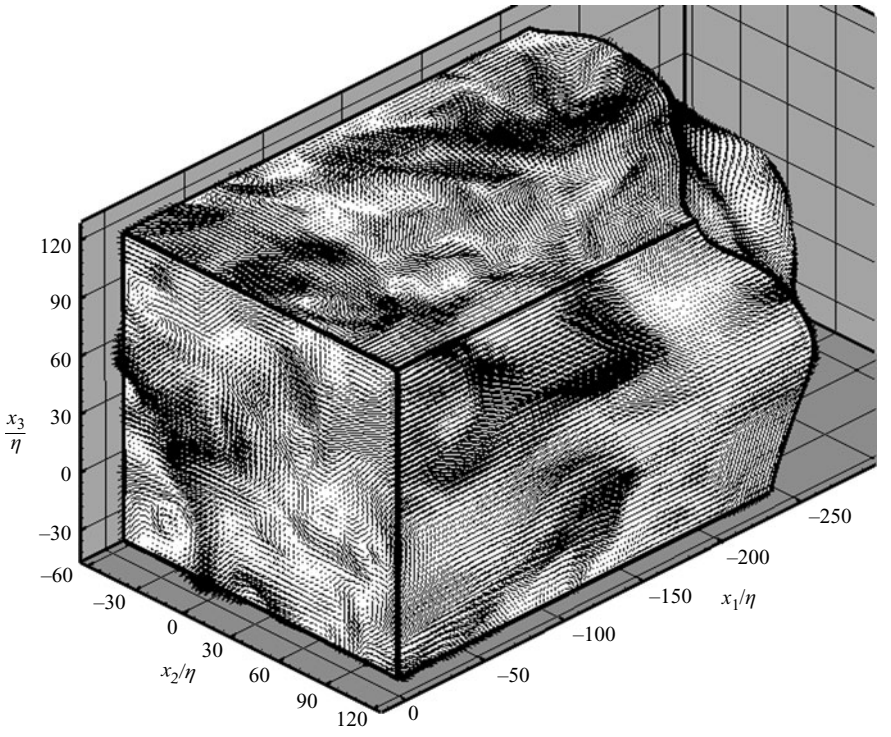

FIGURE 2. Sample vector field from a quasi-instantaneous space–time volume. Only a part of the entire volume is shown. The size of the volume in outer units is $0.8\delta_{1/2} \times 0.6\delta_{1/2} \times 0.6\delta_{1/2}$. Only every other vector is shown for clarity.

stereoscopic vector fields is about $3\eta \times 3\eta$ ($1.35 \times 1.35\,\mathrm{mm}^2$) and successive vectors are separated by 1.5η (due to 50% overlap). The total field size is $76 \times 76\,\mathrm{mm}^2$ ($160\eta \times 160\eta$).

Taylor's hypothesis with a convection velocity equal to the local mean axial velocity $\overline{u_1}(x_2, x_3)$ (u_1, u_2 and u_3 are velocity components along the x_1, x_2 and x_3 directions respectively) was utilized to reconstruct a quasi-instantaneous space–time volume of data. The convection velocity (i.e. the mean axial velocity) varies over the x_2–x_3 plane and consequently the axial coordinates are different for different regions of the jet. The total size of the reconstructed quasi-instantaneous volume is $x_1 \times x_2 \times x_3 = 1300\eta \times 160\eta \times 160\eta$ ($5\delta_{1/2} \times 0.6\delta_{1/2} \times 0.6\delta_{1/2}$). Figure 2 shows three-dimensional velocity vectors from a sample part of the total volume. The field of view of the volume in figure 2 is $250\eta \times 160\eta \times 160\eta$ ($0.8\delta_{1/2} \times 0.6\delta_{1/2} \times 0.6\delta_{1/2}$). The figure clearly shows a distorted grid conforming to the variations in the local convection velocity. The axial coordinates near the jet centre are stretched while the coordinates away from the jet centreline (at larger radial locations) are compressed, since the mean jet axial velocity ($\overline{u_1}$) is higher near the centre and is lower at the periphery.

Energy and dissipation spectra computed from the quasi-instantaneous volume indicate that measurement noise affects the quality of data at high wavenumbers. Therefore, a Gaussian smoothing filter with a filter width of $l_f = 3\eta$ was used to filter the data along all the three directions. This filter width was chosen to match the PIV interrogation window size of 3η to minimize loss of resolution in the cross-stream directions. The use of a Gaussian filter with width of 3η is consistent with filtering

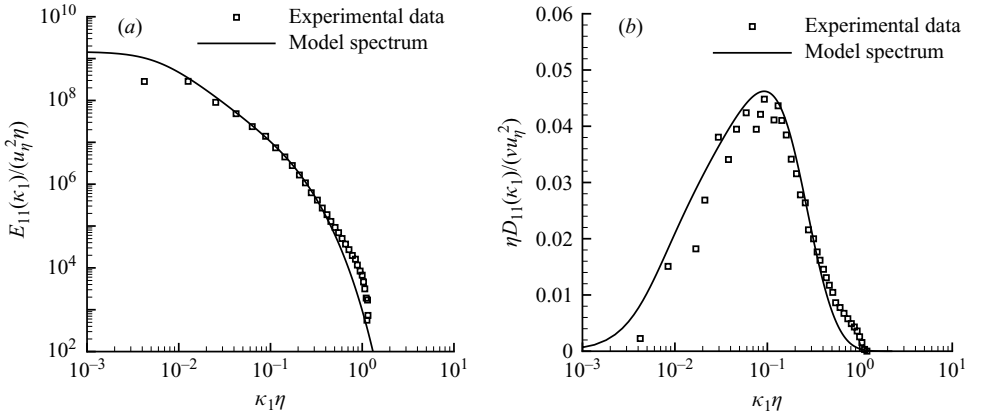

FIGURE 3. Comparison of experimental data with model energy and dissipation spectra (from Pope 2000). The model spectra were computed for $Re_\lambda \approx 150$. (*a*) Energy spectra and (*b*) dissipation spectra.

the data at approximately $2f_\eta$ (where $f_\eta = \overline{u_1}/2\pi\eta$ is the Kolmogorov frequency and is used as the filter frequency in almost all point measurement techniques) and should therefore capture the velocity gradients accurately.

Figure 3(*a*) shows the energy spectrum of axial velocity E_{11} along the κ_1 direction, where κ_1 is the wavenumber in the axial direction (the wavenumber is defined as $\kappa_1 = 2\pi/\Lambda_1$ with units of radians/length, where Λ_1 is the wavelength in the axial direction). Note that the variation in convection velocity over the 'end-view' plane is ignored while computing the axial wavenumbers to simplify the process. A constant convection velocity $\overline{u_1} = 0.66\,\mathrm{m\,s^{-1}}$ (this is the mean axial velocity over the plane) is used to convert frequency to wavenumber in the axial direction.

Pope (2000) proposed a model spectrum of the form

$$E(\kappa) = C\epsilon^{2/3}\kappa^{-5/3} f_L(\kappa L) f_\eta(\kappa\eta), \tag{2.1}$$

where $E(\kappa)$ is the energy spectrum as a function of three-dimensional wavenumber κ ($\kappa = 2\pi/\Lambda$, where Λ is the length scale that corresponds to κ). f_L and f_η are non-dimensional functions whose forms can be found in Pope (2000). The one-dimensional energy spectrum along the κ_1 direction can be computed as

$$E_{11}(\kappa_1) = \int_{\kappa_1}^{\infty} \frac{E(\kappa)}{\kappa}\left(1 - \frac{{\kappa_1}^2}{\kappa^2}\right)\mathrm{d}\kappa. \tag{2.2}$$

Figure 3(*a*) also shows the one-dimensional model spectra $E_{11}(\kappa_1)$ computed from the above-mentioned model. The figure shows that the data follow the model spectra from Pope (2000), further validating the quality of the quasi-instantaneous data.

The one-dimensional dissipation spectrum can be derived from the energy spectrum as $D_{11} = 2\nu{\kappa_1}^2 E_{11}$. The dissipation spectrum shown in figure 3(*b*) is consistent with the dissipation spectrum computed from the model. The general shape and features of the one-dimensional dissipation spectrum in figure 3(*b*), including the peak around $\kappa_1\eta \approx 0.1$, is consistent with spectra in various other studies in the literature (see Antonia, Satyaprakash & Hussain 1982; Saddoughi & Veeravalli 1994; Mi & Nathan 2003).

The filtered pseudo-volume data were used to compute all nine components of the velocity gradient tensor. A second-order central difference technique was employed

i	u_i (m s^{-1})	$\partial u_i/\partial x_1$ (s^{-1})	$\partial u_i/\partial x_2$ (s^{-1})	$\partial u_i/\partial x_3$ (s^{-1})	ω_i (s^{-1})
1	0.19	19.9	24.1	25.4	35.4
2	0.13	23.2	16.2	23.0	38.2
3	0.13	23.5	21.6	16.2	37.1

TABLE 1. Root-mean-square (r.m.s.) statistics of three velocity components, nine velocity gradients and three vorticity components. The vorticity components along the x_1, x_2 and x_3 directions are given by ω_1, ω_2 and ω_3 respectively.

to compute all gradients. Additional details of the experimental technique and its validation for the purpose of computing all nine components of the velocity gradient tensor can be found in Ganapathisubramani, Lakshminarasimhan & Clemens (2006) and Ganapathisubramani, Lakshminarasimhan & Clemens (2007).

3. Statistical results

3.1. *Velocity gradient statistics*

Mean and root-mean-square (r.m.s.) statistics of all three velocity components from the cinematographic stereoscopic data were computed from 2000 vector fields. The (r.m.s.) values listed in table 1 were found to be in agreement with independent hot-wire measurements from Tsurikov (2003) and two-component 'side-view' (x_1–x_2 plane) PIV measurements performed at the same downstream axial location by Ganapathisubramani *et al.* (2006).

Table 1 also lists the (r.m.s.) statistics of all nine velocity gradients computed from the quasi-instantaneous space–time volume. The (r.m.s.) of the velocity gradients do not satisfy local isotropy conditions, especially along the mean-flow direction. Previous studies in the literature have also reported the failure of experimental data to satisfy local isotropy conditions especially along the mean-flow direction. George & Hussein (1991) reported that the homogeneous isotropic conditions do not describe experimentally obtained derivative moments in the far field of circular jets and plane jets. The authors noted that the data instead conformed to axisymmetric isotropy conditions that require that the following ratios are all equal to 1:

$$M_1 = \overline{\left(\frac{\partial u_1}{\partial x_2}\right)^2} \Big/ \overline{\left(\frac{\partial u_1}{\partial x_3}\right)^2}, \tag{3.1}$$

$$M_2 = \overline{\left(\frac{\partial u_2}{\partial x_1}\right)^2} \Big/ \overline{\left(\frac{\partial u_3}{\partial x_1}\right)^2}, \tag{3.2}$$

$$M_3 = \overline{\left(\frac{\partial u_2}{\partial x_2}\right)^2} \Big/ \overline{\left(\frac{\partial u_3}{\partial x_3}\right)^2}, \tag{3.3}$$

$$M_4 = \overline{\left(\frac{\partial u_2}{\partial x_3}\right)^2} \Big/ \overline{\left(\frac{\partial u_3}{\partial x_2}\right)^2}, \tag{3.4}$$

where x_1 is the preferred flow axis (mean-flow direction). Antonia, Kim & Browne (1991) identified the same issue in a DNS dataset of a turbulent boundary layer. The velocity derivatives in the current study are at worst within 10 % of the axisymmetric isotropy conditions. It must be noted that axisymmetric isotropy conditions are

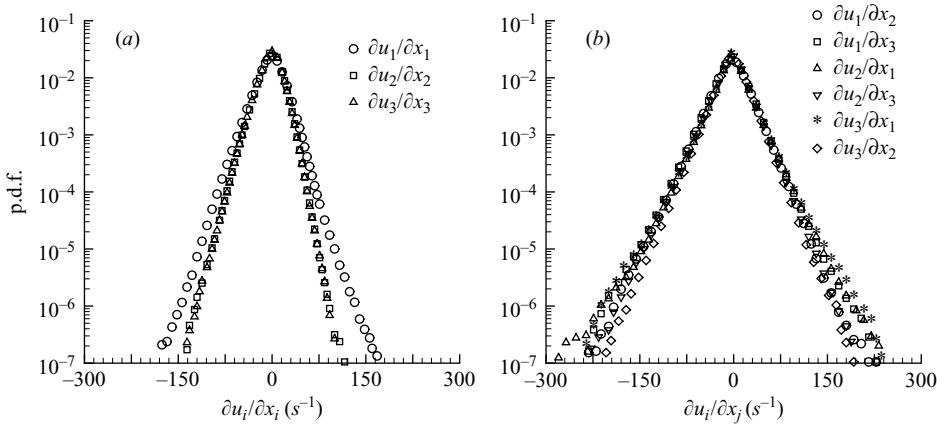

FIGURE 4. Probability density functions of velocity gradients. (*a*) Diagonal components and (*b*) Off-diagonal components.

a subset of conditions required to satisfy homogeneous local isotropy, and the inability of the velocity gradients along the mean-flow direction (especially the velocity component along the mean-flow direction) to satisfy the complete set of homogeneous local isotropy conditions led to the advent of axisymmetric isotropy conditions (George & Hussein 1991).

The r.m.s. values of all three vorticity components computed from the time-resolved stereoscopic data (see table 1) also satisfy the axisymmetric isotropy estimates to within 5 %, which is consistent with results from previous experimental studies by George & Hussein (1991) and computational studies by Antonia *et al.* (1991).

The mean kinetic energy dissipation rate ($\overline{\epsilon}$) was computed using all nine components of the gradients and was found to be 0.069 $m^2\,s^{-3}$. The mean dissipation computed based on axisymmetric conditions (equation 59 in George & Hussein 1991) is $\overline{\epsilon} = 0.066\,m^2\,s^{-3}$. This value is within 5 % of the mean dissipation ($\overline{\epsilon}$) computed from the dataset.

Further analysis of the deviation from local isotropy of the velocity gradients was performed by computing probability distributions of the velocity gradients. Figures 4(*a*) and 4(*b*) show p.d.f.s of the diagonal components and off-diagonal components of the velocity gradient tensor respectively. The diagonal components in figure 4(*a*) show that the axial gradient of the axial velocity component ($\partial u_1/\partial x_1$) exhibits differences compared to the other two diagonal components ($\partial u_2/\partial x_2$ and $\partial u_3/\partial x_3$), indicating deviation from local isotropy. Figure 4(*b*) shows the p.d.f.s of off-diagonal components that appear to collapse for low-gradient values, but exhibit a modest spread for large magnitudes (spread $\approx 100\,s^{-1}$).

All the p.d.f.s reveal a straight-line decay in semi-logarithmic axes on either side of zero consistent with exponential scaling at large values of these gradients. The presence of exponential tails is consistent with previous experimental and computational studies (for example, Sreenivasan & Antonia 1997). The exponential constants can be determined for both left and right tails by computing

$$a = -\frac{\mathrm{d}}{\mathrm{d}|q|}\log P(q), \tag{3.5}$$

where a is the slope of the straight line (in semi-log axes), q is any velocity gradient and $P(q)$ is the probability density function of that velocity gradient. The scaling

a	$\partial u_1/\partial x_1$	$\partial u_1/\partial x_2$	$\partial u_1/\partial x_3$	$\partial u_2/\partial x_1$	$\partial u_2/\partial x_2$	$\partial u_2/\partial x_3$	$\partial u_3/\partial x_1$	$\partial u_3/\partial x_2$	$\partial u_3/\partial x_3$
left	0.069	0.058	0.054	0.059	0.088	0.059	0.058	0.064	0.09
right	0.086	0.062	0.059	0.058	0.124	0.063	0.058	0.067	0.125

TABLE 2. Scaling exponents of left and right tails of the velocity gradients.

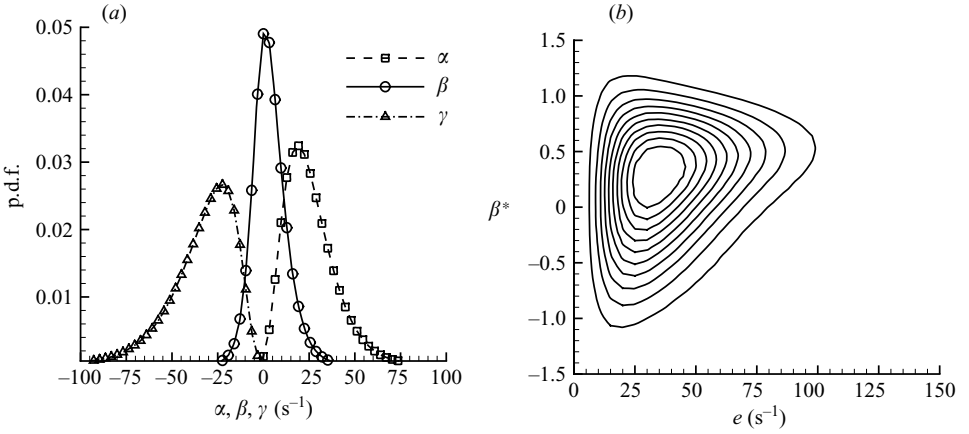

FIGURE 5. (*a*) Probability density functions of all three principal strain rates and (*b*) joint p.d.f. between normalized intermediate strain β^* and magnitude of strain-rate tensor e. Contours from 0.001 to 0.01 are shown in increments of 0.001.

exponents for the left and right tails were computed using a least-squares fit and are listed in table 2. It can be seen from the values in table 2 that there are differences between left and right scaling exponents for the diagonal terms. The differences in the exponents in the off-diagonal components are smaller compared to the diagonal components. The observed differences in the scaling exponents could be due to departure from local isotropy and is consistent with the work of Mullin & Dahm (2006*a*), who also reported similar differences in the scaling exponents of left and right tails.

3.2. *Strain-rate tensor, vorticity and dissipation*

Statistical studies of the strain-rate tensor were carried out by calculating probability distributions and joint probability distributions of all three principal strain-rates. The principal strain rates at every point in the space–time volume were calculated by computing the three eigenvalues of the strain-rate tensor (α, β and γ). The eigenvalues were ordered in magnitude as $\alpha > \beta > \gamma$. Figure 5(*a*) shows the probability distributions of all three principal strains. The general characteristics of the p.d.f.s are consistent with the p.d.f.s of principal strain rates derived from different experimental techniques in other studies in the literature (for example, see Su & Dahm 1996; Mullin & Dahm 2006*b*). Figure 5(*a*) clearly shows that γ strain (compressive strain) has a longer tail than α strain (extensive strain), suggesting that the compressive strain attains larger magnitudes compared to the extensive strain. The distribution of β strain shows that it has a longer tail for $\beta > 0$ compared to $\beta < 0$ to counter the differences between the magnitudes of α and γ.

Betchov (1956) suggested that the intermediate strain (β), which can be positive or negative, determines the local topology of the flow. When β is negative, there are two

directions of compression and the flow field tends to possess line-like topology, and when β is positive, there are two directions of extension and the local flow field has sheet-like structures.

The normalized intermediate strain $\beta^* = \sqrt{6}\beta/e$ (where $e = \sqrt{\alpha^2 + \beta^2 + \gamma^2}$ is the magnitude of the strain-rate tensor) was computed to further study the distribution of the intermediate strain. Figure 5(*b*) shows the joint probability distribution between β^* and e. The figure indicates that the intermediate strain becomes more positive for large values of strain. The mean value of β^* approaches 0.5 with increasing strain-rate magnitude, and this observation is consistent with the findings of Ashurst *et al.* (1987) in a DNS study of isotropic turbulence. This suggests that regions of high strain rate tend to be sheet-forming. The shape of the strain-rate tensor was further investigated by computing averages of α and γ principal strains conditioned on $\beta > 0$. This calculation indicates that, for intense strain values, the strain-rate tensor is in the form $\alpha : \beta : \gamma = 2.9 : 1 : -3 : 8$, which is consistent with DNS results of Ashurst *et al.* (1987) and Lund & Rogers (1994) and experimental results based on hot-wire measurements by Tsinober, Kit & Dracos (1992).

For an incompressible flow (i.e. traceless velocity gradient tensor), the value of β^* should be bounded by ± 1, by definition (see Betchov 1956; Ashurst *et al.* 1987). However, figure 5(*b*) shows that the value of β^* extends to ± 1.5 due to the divergence error present in the data. This divergence error arises from various sources of uncertainty present in the determination of the velocity gradient tensor. (This includes measurement uncertainty, finite differencing errors, error in application of Taylor's hypothesis, etc. See Ganapathisubramani *et al.* 2007 for details.)

The effect of divergence error on β^* can be explored by removing the divergence error from the data using a simple correction scheme. The divergence error was assumed to be distributed equally among the principal strain rates. An equal amount of the error was subtracted from each of the principal strain rates to obtain a traceless velocity gradient tensor. It must be noted that this assumption that the divergence error is isotropic may not be accurate. The fact that the uncertainty in gradients of out-of-plane velocity is larger than the uncertainty in other velocity gradients could result in anisotropic distribution of the divergence error. Moreover, various other correction schemes can also be used to obtain divergence-free data. Regardless, the above-mentioned implementation will provide some basic information on the effects of divergence error on β^*.

Figure 6 shows p.d.f.s of β^* computed using the original experimental data and with the corrected data (i.e. divergence-free data). The figure shows that the p.d.f.s computed using the original data extends to ± 1.5. The p.d.f.s of β^* computed with the transformed data is bounded by ± 1, indicating that the bounds indeed depend on the divergence error. The peak in the p.d.f.s shifts to a higher positive value from $\beta^* = 0.4$ (original data) to 0.5 (divergence-free data). Additionally, the two p.d.f.s exhibit quantitative differences for positive values of β^*. These results are consistent with those obtained by Lund & Rogers (1994), where they examined the effects of experimental uncertainty on β^* by adding isotropic divergence errors to DNS data.

Lund & Rogers (1994) noted that the removal of the divergence error may provide the correct qualitative behaviour, but the quantitative information may still be incorrect. Since the contributions from individual velocity gradients to the divergence error is not known, removing the error equally from the principal strain rates is not necessarily accurate. Therefore, the results to follow are presented without correcting for the divergence error because the assumption that the error is isotropically distributed, if wrong, could lead to incorrect conclusions being drawn from the data.

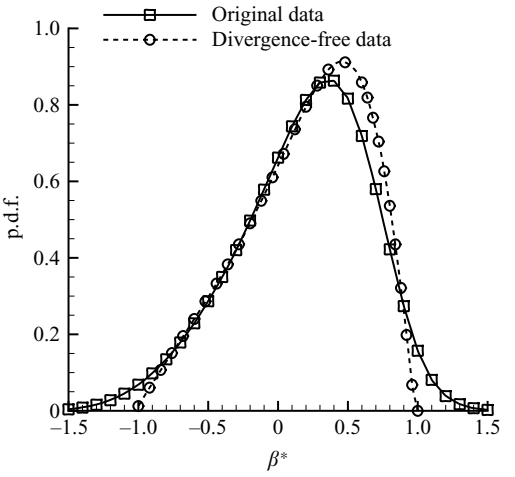

FIGURE 6. Probability density functions of β^*. The solid line (square symbols) shows the p.d.f. of β^* computed with the original experimental data. The dashed line (circle symbols) show the p.d.f. of β^* computed using divergence-free data. The divergence error is removed by a simple transformation where the error is isotropically subtracted from the principal strain rates.

Ganapathisubramani *et al.* (2007) investigated the effect of divergence error on the data and concluded that the error makes a significant impact only in the regions of low gradient/strain values. They concluded that the relative uncertainty in areas of intense gradients is minimal and therefore the data accurately represents those regions of large gradients.

The alignment of the vorticity vector with the strain-rate tensor is investigated by computing the dot product of the strain-rate eigenvectors with the unit vector along the direction of vorticity ($\hat{\boldsymbol{\omega}} = \boldsymbol{\omega}/|\boldsymbol{\omega}|$, where $\boldsymbol{\omega} = \omega_1 \hat{\boldsymbol{x}}_1 + \omega_1 \hat{\boldsymbol{x}}_2 + \omega_1 \hat{\boldsymbol{x}}_3$ is the vorticity vector). Since the eigenvector gives a line in space and not a direction along a line, only the absolute value of the dot product is considered. Figure 7(*a*) shows the alignment p.d.f. of vorticity with the eigenvectors of all the three principal strain rates (i.e. the p.d.f. of $\cos\phi = |\hat{\boldsymbol{e}} \cdot \hat{\boldsymbol{\omega}}|$, where $\hat{\boldsymbol{e}}$ is the eigenvector along either α, β or γ). The extreme values of $\cos\phi = 0$ and 1 (i.e. $\phi = 90^\circ$ and 0°, where ϕ is the angle between the unit eigenvector and the unit vorticity vector), correspond to the vorticity vector perpendicular to the eigenvector and the vorticity vector aligned with the direction of the eigenvector, respectively. Figure 7(*a*) shows that the vorticity vector is most likely to be aligned with the intermediate strain (i.e. maximum in p.d.f. for $\hat{\boldsymbol{\beta}} \cdot \hat{\boldsymbol{\omega}}$ is at $\cos\phi = 1$), which is consistent with previous studies (Ashurst *et al.* 1987; Tao, Katz & Meneveau 1999; Mullin & Dahm 2006*b*). The figure also shows that the vorticity vector is least likely to point in the compressive strain direction. In fact, the p.d.f. of $\hat{\boldsymbol{\gamma}} \cdot \hat{\boldsymbol{\omega}}$ shows a peak at $\cos\phi = 0$, which suggests that the most likely orientation of the vorticity vector is perpendicular to the principal compressive strain. The p.d.f. of $\hat{\boldsymbol{\alpha}} \cdot \hat{\boldsymbol{\omega}}$ is relatively flat and indicates that the vorticity vector does not have a preferred orientation with respect to the largest extensive strain.

Further analysis of the preferred alignment of the vorticity vector can be carried out by computing the joint p.d.f. between $\hat{\boldsymbol{\beta}} \cdot \hat{\boldsymbol{\omega}}$ and the magnitude of vorticity (square root of enstrophy). Figure 7(*b*) shows the above-mentioned joint p.d.f., which reveals that regions of intense enstrophy tend to align with the direction of intermediate strain ($\cos\phi \approx 1$). This observation is consistent with previous results obtained from

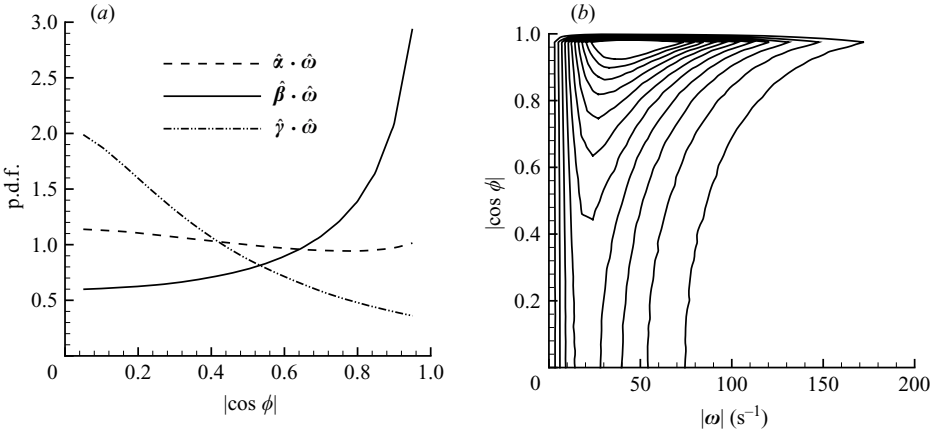

FIGURE 7. (*a*) Probability density functions of the orientation of vorticity vector with eigenvectors of the strain-rate tensor. (*b*) Joint p.d.f. between magnitude of vorticity and orientation of vorticity with the eigenvector corresponding to the intermediate strain ($|\cos\phi| = |\hat{\boldsymbol{\beta}} \cdot \hat{\boldsymbol{\omega}}|$). Contours from 0.003 to 0.03 with a spacing of 0.003.

both experimental and computational studies (Ashurst *et al.* 1987; Ruetsch & Maxey 1992; Tsinober, Shtilman & Vaisburd 1997). This preferred alignment is found for all values of intermediate strain.

The structure of dissipation can be investigated by computing p.d.f.s of $\epsilon = 2\nu s_{ij}s_{ij} = 2\nu e^2$ (where $s_{ij} = 0.5(\partial u_i/\partial x_j + \partial u_j/\partial x_i)$, is the strain-rate tensor). Most experimental studies compute a one-dimensional mean dissipation estimate based on point measurement techniques ($\epsilon_{1D} = \nu(\partial u_1/\partial x_1)^2$: for example, see Antonia, Satyaprakash & Hussain 1980, 1982; Saddoughi & Veeravalli 1994), or a two-dimensional estimate based on planar velocity measurements where only four in-plane velocity gradients are available (see Saarenrinne & Piirto 2000; Saarenrinne, Piirto & Eloranta 2001; Tsurikov 2003). In the current study, the complete velocity gradient tensor was used to compute dissipation (i.e. $\epsilon = \epsilon_{3D}$). Figure 8(*a*) shows p.d.f.s of dissipation computed using the local isotropy assumptions (ϵ_{1D}), dissipation computed using only the velocity gradients in the x_1–x_2 plane (ϵ_{2D}, which is analogous to the dissipation computed in numerous two-component PIV-based studies), and dissipation computed using the entire velocity gradient tensor (ϵ_{3D}). Kolmogorov (1962) postulated a log-normal distribution for kinetic energy dissipation to account for the internal intermittency of turbulence. Although some researchers have shown that this is inconsistent with the physics of incompressible flow (e.g. see Frisch 1995), experimental and computation data of kinetic energy dissipation in the literature seem to follow the log-normal distribution.

Figure 8(*a*) compares the three dissipation rates (ϵ_{1D}, ϵ_{2D} and ϵ_{3D}) with the log-normal distribution. The log-normal model is defined as

$$P(\epsilon^*) = \frac{1}{\sqrt{2\pi}S\epsilon^*}\exp\left(-\frac{(\ln\epsilon^* - M)^2}{2S^2}\right), \tag{3.6}$$

where ϵ^* is the non-dimensional form of kinetic energy dissipation (normalized by its mean value; the mean values of ϵ_{1D}, ϵ_{2D} and ϵ_{3D} are listed in table 2). M and S are constants that can be adjusted to fit the log-normal model to the p.d.f.s. Figure 8(*a*)

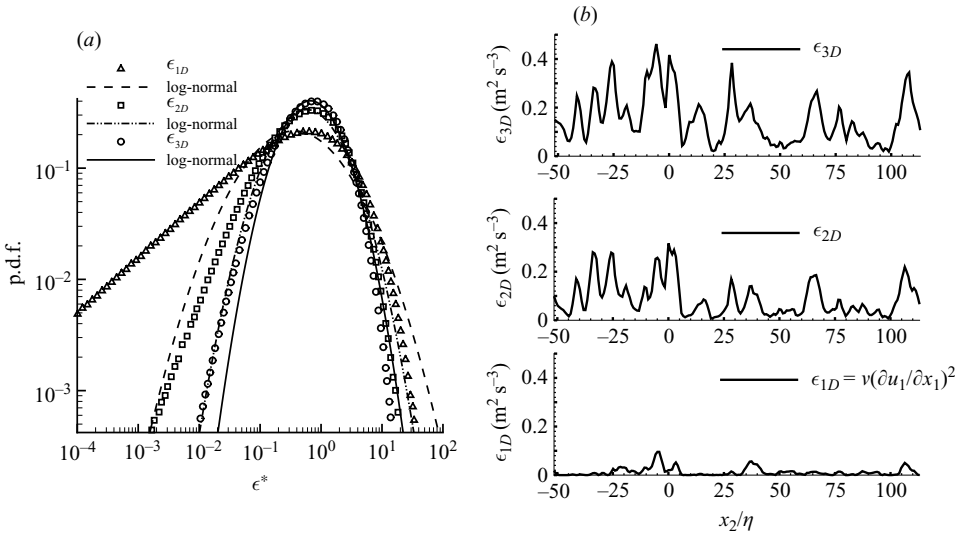

FIGURE 8. (*a*) Probability density functions of $\epsilon_{1D}/\overline{\epsilon_{1D}}$, $\epsilon_{2D}/\overline{\epsilon_{2D}}$ and $\epsilon_{3D}/\overline{\epsilon_{3D}}$. The values of mean dissipation are listed in table 2. The figure also shows a least-squares fitted log-normal distribution for the three p.d.f.s. (*b*) Instantaneous profiles of ϵ_{1D}, ϵ_{2D} and ϵ_{3D} along the x_2 direction.

Parameter	Mean value (m^2 s^{-3})	S	M
ϵ_{1D}	0.006	1.54	1.37
ϵ_{2D}	0.045	1.11	0.68
ϵ_{3D}	0.065	0.94	0.49

TABLE 3. Mean values of dissipation rates and the constants for the log-normal model.

shows the log-normal curve fits for all three dissipation rates. The log-normal model appears to be a relatively good fit for the p.d.f. of ϵ_{3D}. This observation is consistent with the observation of Mullin & Dahm (2006*b*), where ϵ_{3D} computed using the dual-plane stereoscopic technique was found to follow the log-normal distribution. The model log-normal distribution seems to be a good approximation for the right side tail of ϵ_{2D}, however, the left tail (i.e. low values of dissipation) deviates from the model. The log-normal approximation clearly does not model the distribution of ϵ_{1D}. The best fit constants for the log-normal model for all three dissipation rates are given in table 2. The values of S and M decreases from ϵ_{1D} to ϵ_{3D}. Both ϵ_{1D} and ϵ_{2D} possess more regions of low dissipation compared to ϵ_{3D} owing to the projection of three-dimensional dissipation structures on to a lower-dimensional space. The presence of a long tail for low values of dissipation suggests that ϵ_{1D} and ϵ_{2D} may not accurately reveal the true characteristics of dissipation.

Figure 8(*b*) shows representative instantaneous profiles of dissipation rates (ϵ_{1D}, ϵ_{2D} and ϵ_{3D}) along the x_2 direction. The figure suggests that ϵ_{1D} tends to underestimate the value and scale of dissipation. Figure 8(*b*) also shows that the two-dimensional form of dissipation, ϵ_{2D}, underestimates the size (length) and peak values of dissipation regions owing to the inclusion of only four terms from the velocity gradient tensor in the computation of dissipation.

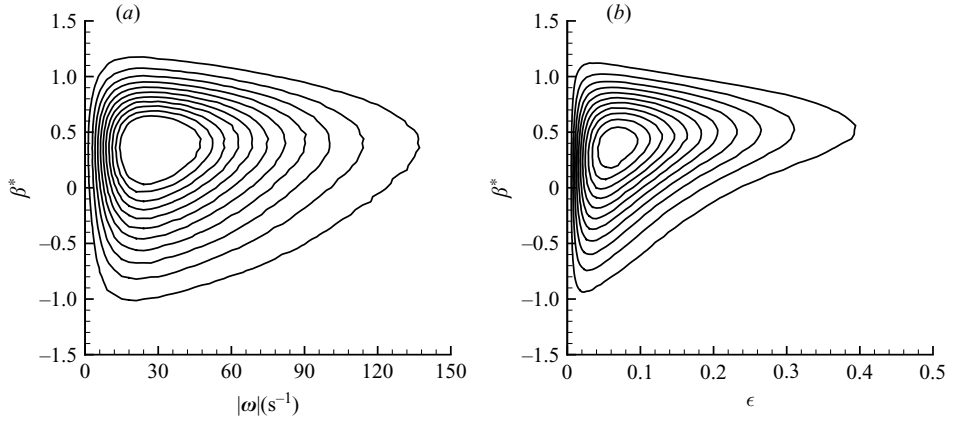

FIGURE 9. (*a*) Joint p.d.f. between magnitude of vorticity ($|\omega|$) and β^*. Contours from 0.001 to 0.01 are shown in increments of 0.001. (*b*) Joint p.d.f. between β^* and ϵ. Contours from 0.005 to 0.05 are shown in increments of 0.005.

Joint p.d.f.s were computed to investigate the relationships between dissipation, vorticity and strain rates. Figure 9(*a*) shows a joint distribution between the norm of the vorticity vector ($|\omega|$) and β^*. This figure indicates that regions of intense vorticity seem to possess a preference for positive β^*, implying that intense vorticity regions are associated with a sheet-forming strain field. This aspect is investigated in greater detail by computing conditional p.d.f.s and is presented later in this section.

Instantaneous plots from DNS results (Siggia 1981; Jimenez *et al.* 1993) show that intense vortex structures are in the form of tubes. Therefore, it would be natural to expect β^* to be negative in the regions of intense vorticity, since a negative intermediate strain would give rise to a line- or tube-forming strain field. However, joint p.d.f.s between enstrophy and β^* indicates that regions of intense vorticity reveal a marginal preference towards positive values of β^* (although the preference exhibited is weaker compared to dissipation, as explained later in this section). Therefore, the presence/formation of vortex tubes might not be simply due to the presence of a favourable strain field and may depend on some unsteady process. This observation is consistent with the model proposed by Ruetsch & Maxey (1991), who indicated that regions of moderate vorticity magnitude appear in the form of sheets, and these sheets, owing to some underlying instability (perhaps Kelvin–Helmholtz), roll up and form tubes of intense vorticity. This process cannot be captured with snapshots of instantaneous information and would require time-resolved three-dimensional information, which could be made available only through computational studies.

Figure 9(*b*) shows the joint p.d.f. between the normalized intermediate strain (β^*) and dissipation (ϵ). The shape of the joint p.d.f. is skewed towards positive values of β^* for intense values of ϵ. The p.d.f. contours inflect towards positive values of β^* for intense values of ϵ, which is marginally different from the joint p.d.f. between $|\omega|$ and β^*, which is more rounded for intense values of $|\omega|$. This suggests that intense values of ϵ have a stronger propensity to occur in regions of positive β^* (compared to $|\omega|$).

The relationships between intermediate strain and dissipation, and intermediate strain and vorticity can be further investigated by computing conditional p.d.f.s of β^*. Figure 10(*a*) shows conditional p.d.f.s of β^*, where the p.d.f.s for various thresholds of $|\omega|/\overline{|\omega|} > 0.5$, 1, 1.5 and 2. The conditional p.d.f.s exhibit no discernible

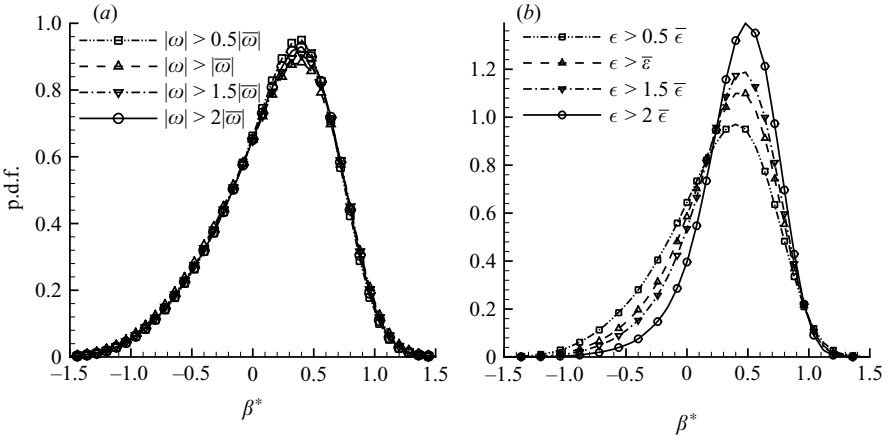

FIGURE 10. (*a*) Probability density functions of β^* conditioned on magnitude of $|\omega|$. Four different thresholds were used: $|\omega| > 0.5$, 1, 1.5 and $2\overline{|\omega|}$. (*b*) Probability density functions of β^* conditioned on magnitude of ϵ. Four different thresholds were used: $\epsilon > 0.5$, 1, 1.5 and $2\overline{\epsilon}$.

difference, indicating that regions of intense vorticity do not necessarily coincide with regions of intense intermediate principal strain rate. The mean value of β^* remains nearly a constant ($\overline{\beta^*} = 0.2$), with increasing thresholds on magnitude of vorticity. This inference is consistent with the previous observations in DNS studies (see Siggia 1981; Jimenez *et al.* 1993), where the structure of regions of intense vorticity was found to be in the form of tubes. The presence of large positive intermediate strain results in two intense extensive principal strains that would tend to stretch the structure into 'sheets', and the fact that the instantaneous vortex structures are in the form of tubes rather than sheets, reinforces the inference based on the conditional p.d.f.s that the presence of intense vorticity does not imply large positive intermediate strain, or vice versa.

Figure 10(*b*) shows the conditional p.d.f.s of β^* for a range of thresholds on ϵ. The threshold on dissipation for the four conditional p.d.f.s were $\epsilon/\overline{\epsilon} > 0.5$, 1, 1.5 and 2. The peaks in the conditional p.d.f.s move towards higher positive values of β^* with increasing threshold. The area under the curve of the conditional p.d.f.s for $\beta^* < 0$ also decreases with increasing threshold. The mean value of β^* increases from 0.2 to 0.5 with increasing value of dissipation threshold, indicating that intense dissipation regions occur in regions of intense positive intermediate strain and is consistent with the DNS results of Ashurst *et al.* (1987) and Lund & Rogers (1994). The strong correlation between intense dissipation and β is in contrast with the behaviour of vorticity, where regions of intense vorticity did not reveal any inclination towards positive or negative regions of β (as seen in figure 10*a*).

4. Instantaneous results

The structure of the strain-rate, vorticity and dissipation fields can be further studied by rendering instantaneous iso-surfaces of β, ω and ϵ over a volume. This analysis is similar to those performed in previous DNS-based studies (Siggia 1981; Yamamoto & Hosokawa 1988; Vincent & Meneguzzi 1991; Jimenez *et al.* 1993).

Figure 5(*a*) in the previous section shows that the p.d.f. of the intermediate strain rate has a longer tail for $\beta > 0$ than for $\beta < 0$, indicating that the intermediate strain

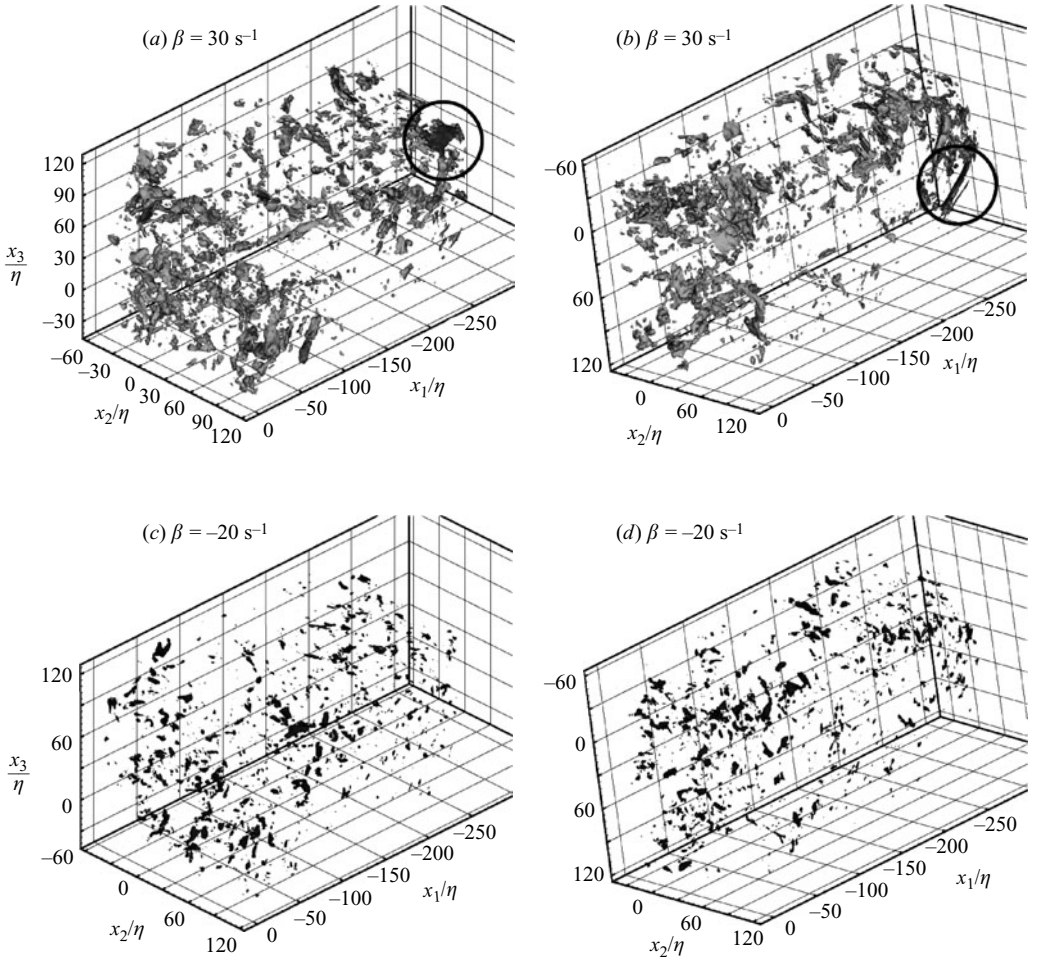

FIGURE 11. Structure of intermediate strain rate. (a, b) Two different perspectives of iso-surfaces of $\beta = 30\,\mathrm{s}^{-1}$. ($c$, d) Two different perspectives of iso-surfaces of $\beta = -20\,\mathrm{s}^{-1}$.

attains larger positive values than negative values. Therefore, the structure of regions of intense strain rate can be investigated by visualizing iso-surfaces of β at two different values (one for $\beta > 0$ and another for $\beta < 0$).

Figures 11(a) and 11(b) show two different perspectives of iso-surfaces of $\beta = 30\,\mathrm{s}^{-1}$, which correspond to structures of intense positive intermediate strain rate (i.e. $\beta = 3\sigma_\beta$, where σ_β is the r.m.s. of the intermediate strain). At this elevated threshold the iso-surfaces of positive intermediate strain reveal coherent structures that seem to be in the form of sheets. A region of intense positive β is marked in figures 11(a) and 11(b). The marked region appears to be a 'blob' in figure 11(a); however, it is clear from figure 11(b) that the structure of that marked region is in fact in the form of a 'sheet'. Investigation of several other individual structures indicates that positive intermediate strain is in the form of sheets. In addition, as will be shown later in this section, these regions of intense positive intermediate strain also coincide with regions of intense dissipation.

Figures 11(c) and 11(d) show two different perspectives of iso-surfaces of $\beta = -20\,\mathrm{s}^{-1}$, which corresponds to structures of intense negative intermediate strain

rate (i.e. $\beta = -2\sigma_\beta$; note the lower threshold for negative intermediate strain). Both figures indicate that intense negative intermediate strain does not possess an extended coherent structure. The iso-surfaces in both figures are 'spotty' and do not extend in any direction. From figure 11, it can be concluded that the sheet-forming strain fields ($\beta > 0$) are organized into sheet-like structures, whereas line-forming strain fields ($\beta < 0$) are organized as smaller-scale spotty structures, not as lines or tubes.

The structure of the vorticity field can be studied by examining the contours/iso-surfaces of a vortex identification parameter that is based on the local flow topology. Various studies in the literature have compared and contrasted several vortex identification parameters (for example, Jeong & Hussain 1995; Cucitore, Quadria & Baron 1999), but there is no general consensus on an optimal parameter to isolate vortex cores. Zhou *et al.* (1999) used swirling strength (λ_{ci}^2), which is the square of the imaginary part of the eigenvalue of the three-dimensional velocity gradient tensor, to visualize vortex cores in a DNS dataset of channel flow. They found that this quantity, which isolates regions of fluid swirling about an axis, can be used to visualize vortical structures. In this study, the swirling strength, defined as $\lambda_{3D} = |\lambda_{ci}|$, is used to visualize swirling regions in the flow. Although swirling strength is used to visualize the structure of swirling/rotational motion, it must be noted that the use of other vortex identification parameters like enstrophy (or alternatively, the second invariant of the velocity gradient tensor or λ_2, as defined in Jeong & Hussain 1995) does not alter the results or conclusions presented in this section. Moreover, previous studies have observed that vortex structures educed by the different criteria using non-zero thresholds are quite similar (for example, see Zhou *et al.* 1999; Dubief & Delcayre 2000; Chakraborty, Balachandar & Adrian 2005).

Figures 12(*a*)–12(*d*) show iso-surfaces of $\lambda_{3D} = 75\,\mathrm{s}^{-1}$ (where mean and r.m.s. values of λ_{3D} correspond to $15\,\mathrm{s}^{-1}$ and $20\,\mathrm{s}^{-1}$ respectively). All the figures show that the vortex structures are organized in tube-like structures, which is consistent with observations made in previous DNS studies (Siggia 1981; Ashurst *et al.* 1987; Ruetsch & Maxey 1992; Jimenez *et al.* 1993). These tube-like structures were named 'worms' by Jimenez *et al.* (1993), who indicated that these 'worms' were the most intense realizations of background vorticity (i.e. the magnitude of vorticity in these tubes is much larger than the root mean square of vorticity).

Further investigation of the size of the 'worms' was conducted by extracting a cross-sectional plane of data normal to the axis of one elongated worm (marked A in figure 12*d*). Figure 12(*e*) shows contours of λ_{3D} in the cross-sectional plane normal to the axis of a 'worm'. The contours indicate a circular profile for the vortex core. Figure 12(*e*) also shows a range of other vortex structures that cut across the plane. Most notably, the cross-section of an elongated tube (marked B) indicates the typical length of these worms to be approximately $60 - 100\eta$. Figure 12(*f*) shows a diametric profile of $\lambda_{3D}/\lambda^m{}_{3D}$ along the line marked in figure 12(*e*) (where $\lambda^m{}_{3D}$ is the maximum value of λ_{3D} within the vortex core). Jimenez *et al.* (1993) used enstrophy ($|\omega|^2$) as the vortex identification parameter to isolate the 'worms' and subsequently fitted a Gaussian shape to the radial distribution of axial vorticity (i.e. vorticity component along the axis of the identified 'worm'). They defined the local radius of the worm as the $1/e$ radius of the Gaussian fitted to axial vorticity. Following the definition proposed by Jimenez *et al.* (1993), the diameter of the core marked A in figure 12(*f*) was computed as twice the $1/e$ radius of the Gaussian shape fitted to λ_{3D} in a plane normal to the axis of the 'worm'. This diameter was found to be 9η. Figure 12(*f*) also reveals diametric profiles of two other structures. The profiles indicate that the core diameters of these structures vary between 8η and 12η. Analysis of other vortex

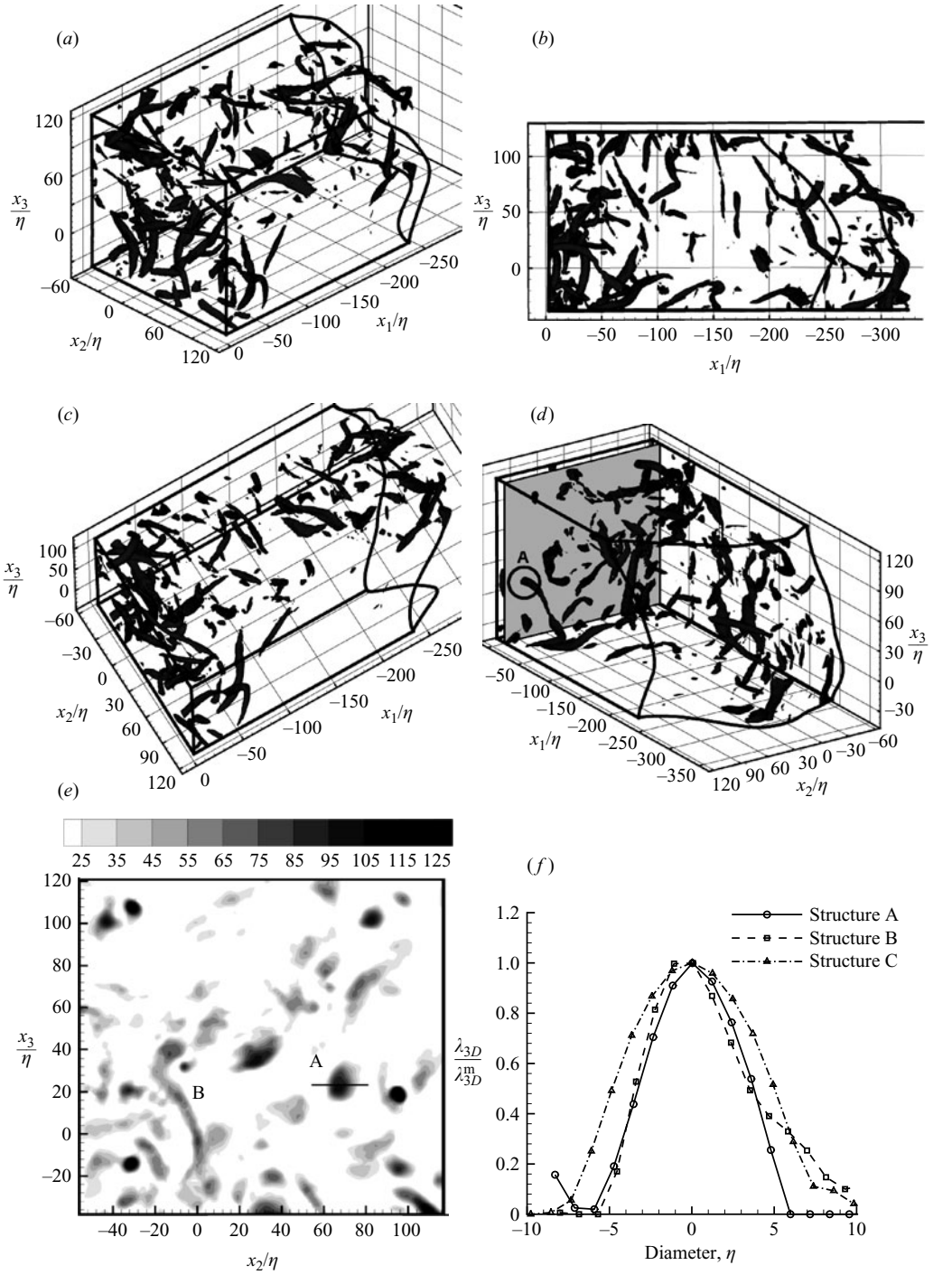

FIGURE 12. Instantaneous vortex structure. (*a*)–(*d*) Different views of iso-surfaces of $\lambda_{3D} = 75\,\mathrm{s}^{-1}$. (*e*) Contours of λ_{3D} on a plane normal to the vortex tube marked A. The plane is shown in figure 12(*d*). (*f*) Swirling strength profiles across selected vortex cores. The profiles are along a diametric line in a plane normal to the axis of the core.

cores indicates that the core diameter varies from 6η to 15η and is consistent with the results of Jimenez *et al.* (1993), who found that the diameter of intense vortex worms was nominally 8η. The observation that the worm core diameter is significantly larger than the Kolmogorov scale is also consistent with the 'strain-limited diffusion scale for vorticity', λ_v, defined by Buch & Dahm (1996). Buch & Dahm (1998) and Mullin & Dahm (2006*b*) inferred from scalar dissipation measurements and dual-plane stereoscopic measurements, respectively, that the smallest scale of vortical structures is λ_v, which is about six times larger than the Kolmogorov scale. This observation is not in agreement with the model proposed by Tennekes (1968), which states that the tube diameter is of order η.

Tsurikov (2003) performed planar PIV in the x_1–x_2 plane (in the same facility used in this study) and found that the kinetic energy dissipation structures possess a wide range of sizes and shapes. However, the conclusions by Tsurikov (2003) were based on planar data and it was not possible to speculate on the three-dimensionality of the structure of dissipation. The reconstructed quasi-instantaneous volume in the present study provides an opportunity to further investigate the three-dimensionality of these dissipative structures. The instantaneous three-dimensional structure of dissipation was investigated by examining iso-surfaces of ϵ. Figure 13(*a*) shows iso-surfaces of $\epsilon = 0.4\,\mathrm{m^2\,s^{-3}}$, which is about six times the value of mean dissipation. Therefore, the iso-surfaces of $\epsilon = 0.4\,(\approx 6\overline{\epsilon})$ represent intense dissipative regions in the flow field. Figure 13(*a*) seems to show a wide range of shapes and forms for the dissipation structure that vary from sheets to blobs. This observation is consistent with the previous studies by Siggia (1981) and Yamamoto & Hosokawa (1988), where three-dimensional visualization of kinetic energy dissipation obtained from DNS data was found to be complex, containing sheet-, line- and blob-like structures.

The structure of dissipation can be examined in detail by isolating individual structures. Consider the three characteristic blobs marked A, B and C in figure 13(*b*). Figures 13(*c*) and 13(*d*) show views of the same blobs A, B and C from two different perspectives. Figure 13(*c*) shows that the blobs A and B are in fact sheet-like structures with finite thickness. Similarly, figure 13(*d*) reveals that the blob marked C also possesses a sheet-like structure. Figures 13(*c*) and 13(*d*) also reveal multiple structures (not marked) that are sheet-like, but appear to be blobs when viewed from other perspectives. Movie sequences generated by rotating the pseudo-volume along different axes reveal that most blobs (seen in figure 13*a*) are in fact sheets. Additionally, the sheets of intense dissipation are also found to coincide with the sheets of intense positive intermediate strain in figures 11(*a*) and 11(*b*).

To further investigate the thickness of the sheets of dissipation, a plane normal to the axis of the dissipation sheet marked C is extracted as shown in figure 13(*d*). This extracted plane (x_a–x_2, x_a is the coordinate along the plane shown in figure 13*e*) is at an angle $\xi = 60^\circ$, where ξ is the angle made by the plane with x_1–x_2 plane. Figure 13(*e*) shows contours of ϵ in the extracted x_a–x_2 plane (the coordinate $x_a = x_3 \sec\xi$). The contours reveal that the dissipation sheet has a finite thickness. The contours also indicate that the largest length scale of these sheets is of order 60–100η. For example, the length of the sheet marked C is approximately 60η in the x_2 direction. The thickness of the dissipation sheet can be deduced by plotting the profile of ϵ along the line marked x_n, in figure 13(*e*). Buch & Dahm (1998) investigated the thickness of scalar dissipation structures and the thickness was determined by the width where the dissipation falls to 20 % of the local maximum value. Following the above-mentioned definition for thickness, the profile, ϵ/ϵ^m versus x_n (where ϵ^m is the maximum value of dissipation in the sheet) in figure 13(*f*) shows that the thickness of sheet C is

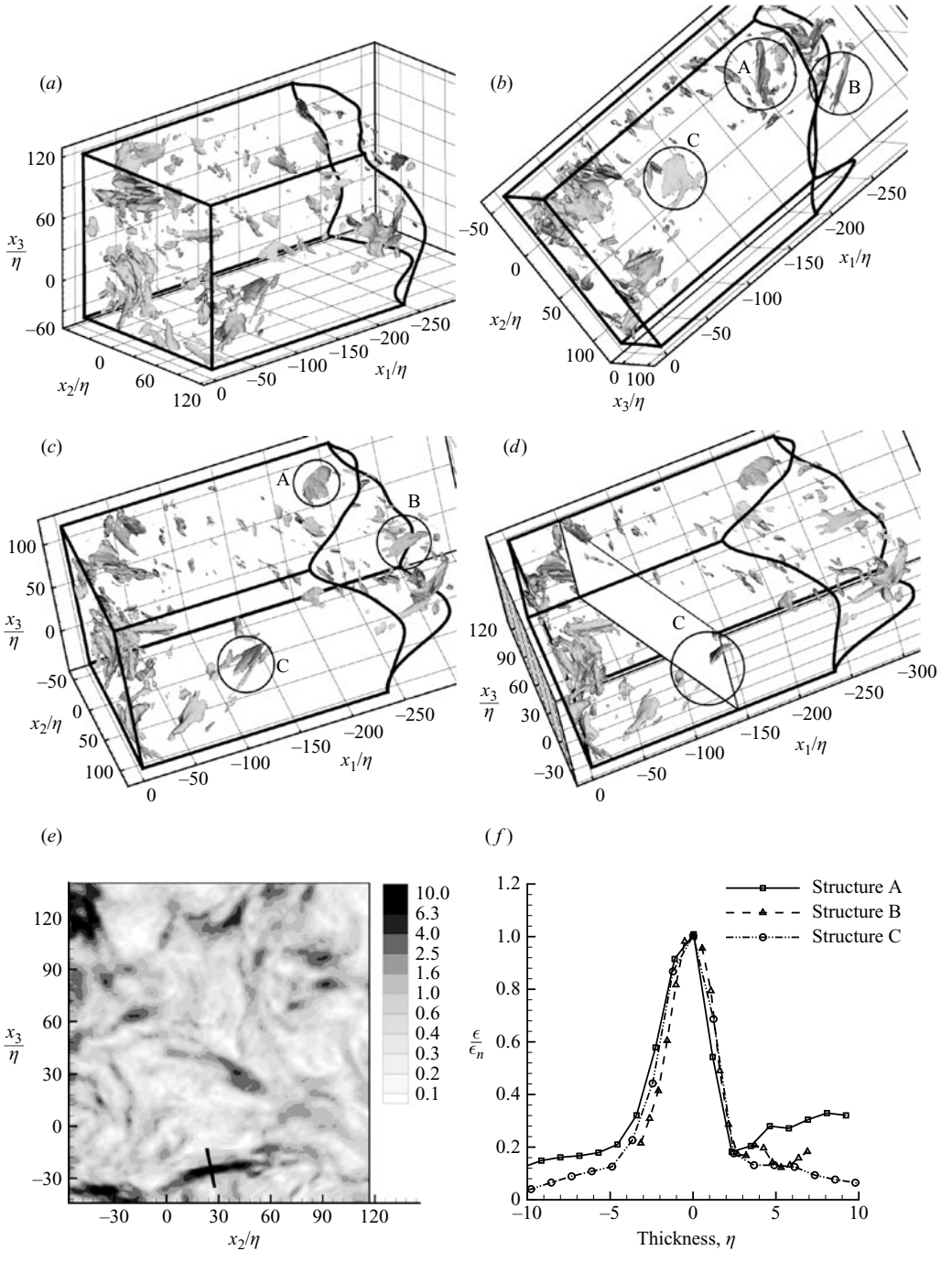

FIGURE 13. Instantaneous dissipation structure. (*a*)–(*d*) Different views of iso-surfaces of $\epsilon = 0.4\,\mathrm{m^2\,s^{-3}}$. (*e*) Contours of ϵ on a plane normal to the dissipation sheet marked C. The dissipation value is normalized by the mean dissipation and contours ranging from $0.1\bar{\epsilon}$ to $10\bar{\epsilon}$ are shown. The plane is shown in figure 13(*d*). (*f*) Thickness profiles of dissipation sheets along a line normal to the structure in a plane that is normal to the sheet.

approximately 10η. Figure 13(f) also shows thickness profiles of structures A and B. These thickness profiles were extracted from planes normal to those structures and they indicate that the thickness of dissipation sheets varies between 8η and 10η. Similar analysis of other sheets of dissipation shows that the thickness nominally varies between 6η and 12η and this result is consistent with the observation made by Tsurikov (2003) based on planar PIV measurements. These observations are also consistent with the findings on scalar dissipation of Ruetsch & Maxey (1992) based on DNS results, who noted that the scalar dissipation structures possess characteristic thicknesses of approximately 5η and a length of approximately 60η.

The iso-surfaces of ϵ and λ_{3D} can be visualized simultaneously to investigate the instantaneous relationship between the vortical and dissipation structures. Figures 14(a) and 14(b) show iso-surfaces of $\epsilon = 0.4\,\mathrm{m^2\,s^{-3}}$ (in blue) and $\lambda_{3D} = 75\,\mathrm{s^{-1}}$ (in gold) from two different perspectives. The figures show that intense dissipative regions are not coincident with regions of intense λ_{3D}: rather, the elongated tubes of intense vorticity are surrounded by the sheets of intense dissipation (Kerr 1985; Vincent & Meneguzzi 1994; Pradeep & Hussain 2006).

The joint p.d.f. between λ_{3D} and ϵ was computed to investigate the concurrence of intense values of the two quantities. Figure 15(a) shows the above-mentioned joint p.d.f. in which the dissipation axis (ordinate) is plotted in logarithmic scale (i.e. $\log\epsilon$) to stretch the axis to low values. The contour levels in the figure range from 10^{-5} to 5×10^{-3} and follow an exponential distribution. The figure indicates a high probability for $\lambda_{3D}=0$ (within the first bin, as marked in the figure) for all values of dissipation. The joint p.d.f. also shows that intense values of ϵ are not correlated with large magnitudes of λ_{3D}. For example, the joint p.d.f. reveals that the probability that λ_{3D} is equal to zero at the location where dissipation is equal to $0.4\,\mathrm{m^2\,s^{-3}}$ is 8×10^{-4}, whereas the probability that λ_{3D} is equal to $75\,\mathrm{s^{-1}}$ at a point where ϵ is equal to $0.4\,\mathrm{m^2\,s^{-3}}$ is approximately 8×10^{-6}. The probability is lower by two orders of magnitude for the higher value of swirling strength. This suggests that intense dissipation very rarely occurs concurrently with intense swirling strength (also observed by Kerr 1985; Vincent & Meneguzzi 1994).

A further quantitative evaluation of this feature was performed by computing the number density of λ_{3D} conditioned on the presence of intense dissipation (number density is defined as the total number of points in the dataset where the condition prescribed is satisfied). Figure 15(b) shows the number densities of λ_{3D} for various thresholds of $\epsilon/\overline{\epsilon} >$ 0, 1.5, 3, 4.5 and 6. The figure indicates that the number of points with large values of λ_{3D} decreases with increasing dissipation threshold, suggesting that intense dissipation is not present in the same areas as intense swirling strength.

Having established that intense dissipation and intense swirling strength are not strongly correlated, a qualitative investigation on their mutual relationship was performed by isolating representative regions that contain both intense swirling strength and dissipation. It is clear that an isolated vortex tube in an otherwise quiescent flow should not be associated with dissipation because solid body rotation is strain-free; however, interactions among multiple tubes could certainly lead to dissipation between and possibly within the tubes. Three different regions where dissipation is found in the vicinity of vortex tubes are marked in figures 14(a) and 14(b). Regions marked A and B possess a nested structure of multiple vortex tubes with crumpled dissipation sheets located between the tubes, whereas the region marked C does not have multiple tubes. Only two vortex tubes and an isolated sheet of dissipation are found in region C. To examine the strength of these isolated sheets, the threshold for dissipation iso-surfaces was increased from $\epsilon = 6\overline{\epsilon}$ to $\epsilon = 10\overline{\epsilon}$.

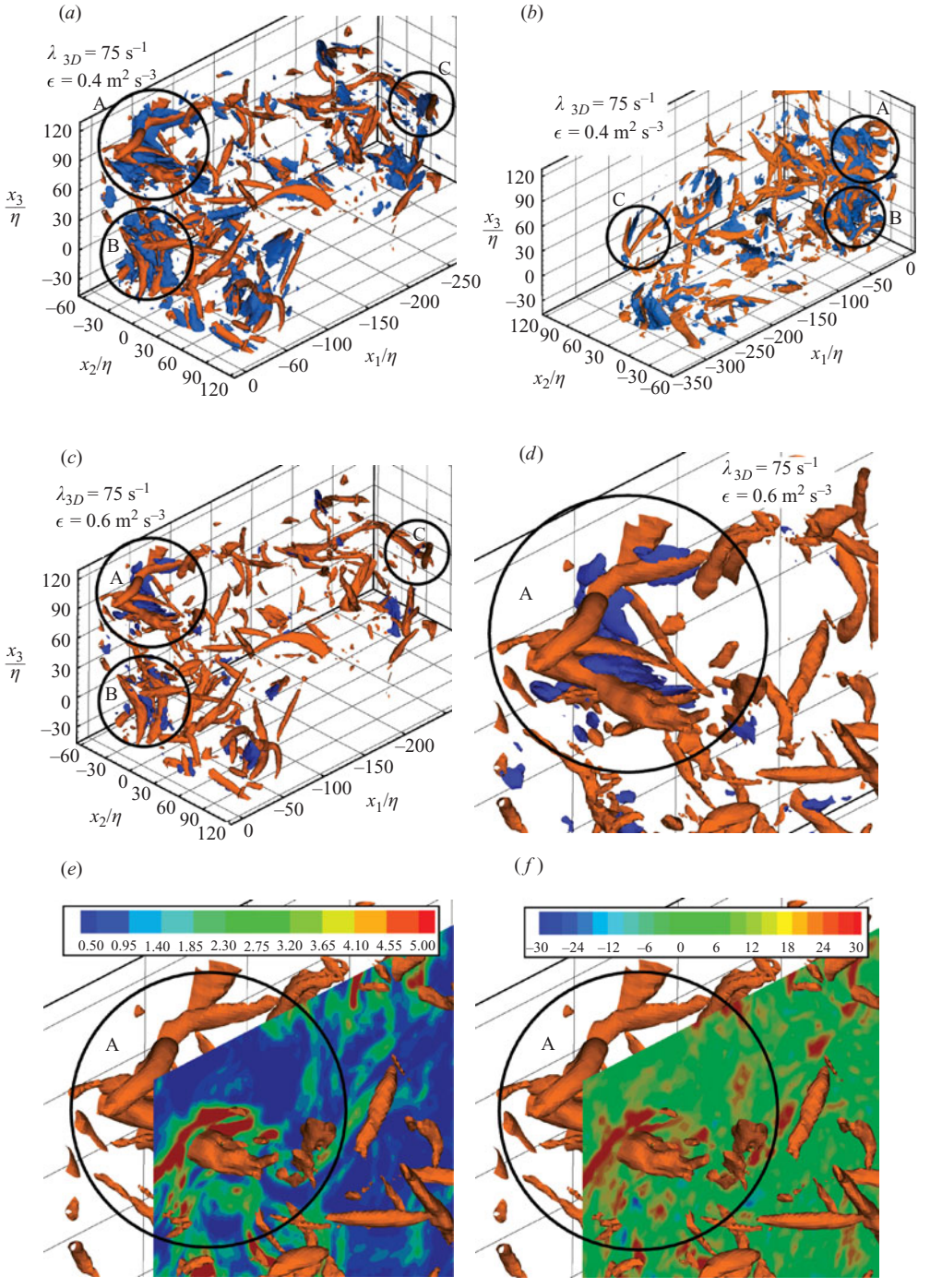

FIGURE 14. (*a*, *b*) Two different perspectives of iso-surfaces of $\lambda_{3D} = 75\,s^{-1}$ and $\epsilon = 0.4(6\overline{\epsilon})$. (*c*) Iso-surfaces of $\lambda_{3D} = 75\,s^{-1}$ and $\epsilon = 0.6\,m^2\,s^{-3}(10\overline{\epsilon})$. (*d*) A closer look at the structure marked A. (*e*) Contours of $\epsilon/\overline{\epsilon}$ in a plane normal to a vortex core; contours ranging from 0.5 to 5 are shown. (*f*) Contours of β strain rate in a plane normal to a vortex core; contours ranging from $-30\,s^{-1}$ to $30\,s^{-1}$ are shown.

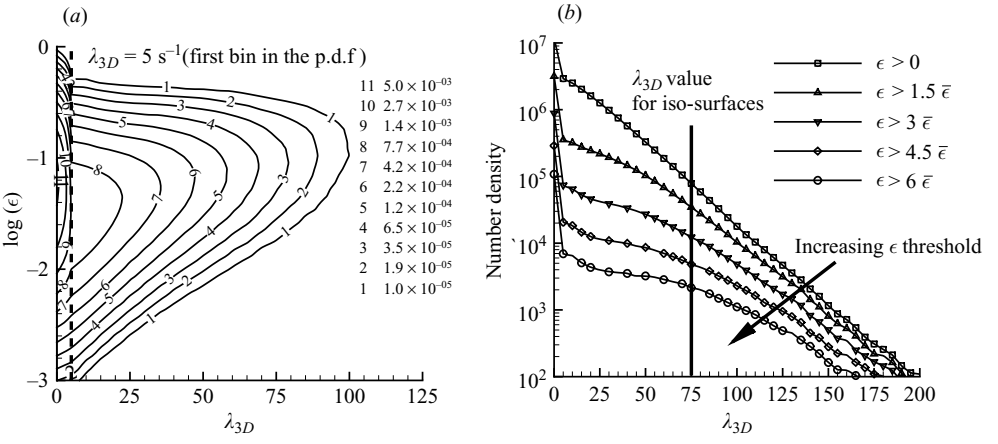

FIGURE 15. (*a*) Joint p.d.f. between swirling strength (λ_{3D}) and dissipation (ϵ). Contours from 1×10^{-5} to 5×10^{-3} are shown and the contour levels are on a logarithmic scale. (*b*) Number densities of λ_{3D} conditioned on ϵ. Five different thresholds were used: $\epsilon/\overline{\epsilon} > 0$, 1.5, 3, 4.5 and 6. The number of points with large values of λ_{3D} decreases with increasing dissipation threshold.

Figure 14(*b*) shows the iso-surfaces for $\lambda_{3D} = 75\,\mathrm{s}^{-1}$ and $\epsilon = 0.6\,\mathrm{m}^2\,\mathrm{s}^{-3}$ ($10\overline{\epsilon}$). This figure indicates that regions of extremely intense dissipation are found predominantly in regions where there are multiple vortex cores. At this elevated threshold, the size of certain dissipation sheets decreases from 60–100η to about 30η, and some other dissipation sheets just disappear. For example, the dissipation sheet marked C is no longer present at this higher threshold. However, the crumpled sheets in regions A and B are present even at this higher threshold (size of approximately 30η). Overall, figures 14(*a*)–14(*c*) indicate that extremely intense dissipative regions occur between multiple vortex tubes where the strain fields induced by these vortex tubes overlap.

Previous computational studies (Kida & Ohkitani 1992; Melander & Hussain 1993; Pradeep & Hussain 2006) have noted that the induced strain rate is maximized in regions between multiple vortex columns/tubes. This is entirely consistent with the above observation where intense dissipative structures are found in areas between tubes of intense vorticity.

The local structure of dissipation around a vortex tube can be further investigated by considering a zoomed-in view of the nested structure marked A in figure 14(*c*). Figure 14(*d*) reveals a closer look at the iso-surfaces of λ_{3D} and ϵ in region A, and indicates that the sheet of dissipation is crumpled and nested between two or more cores. Contours of ϵ in a cross-sectional plane normal to a vortex core is shown in figure 14(*e*) (figure 16*a* shows the same dissipation field in grey-scale without the iso-surfaces of vortex cores, for the sake of comparison). The contours show that the dissipation structure around the vortex core is in the form of an annulus; however, the annular region is not radially symmetric. This observation is consistent with the findings of other DNS-based studies, where visualization of isotropic turbulence indicated that moderate dissipation tended to surround the vortex tubes (Kerr 1985; Brachet 1991; Vincent & Meneguzzi 1994). Figure 14(*f*) shows contours of intermediate strain rate (β) in the same cross-sectional plane (figure 16*b* shows the same intermediate strain field in grey-scale, without the iso-surfaces of vortex cores). The figure indicates that the intermediate strain possesses intense positive values in the regions of intense dissipation consistent with the findings based on joint and conditional p.d.f.s in the previous section. This provides further

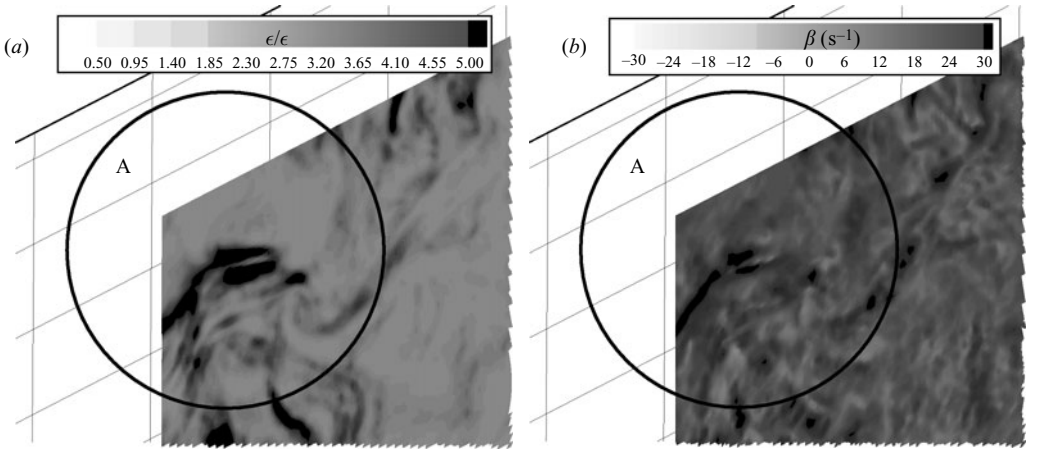

FIGURE 16. (*a*) Contours of $\epsilon/\bar{\epsilon}$ in a plane normal to a vortex core; contours ranging from 0.5 to 5 are shown. (*b*) Contours of β strain rate in a plane normal to a vortex core; contours ranging from $-30\,\mathrm{s}^{-1}$ to $30\,\mathrm{s}^{-1}$ are shown. (*a*) and (*b*) are identical to figures 14(*e*) and 14(*f*), respectively; however, the iso-surfaces of vortex tubes are not shown here for the sake of comparison.

support for the presence of sheet-like intense dissipative structures, since the sheet structure is induced by the presence of two extensive strains. It should also be noted from figures 14(*d*) and 14(*e*) (in liaison with figures 16*a* and 16*b*) that neither β nor ϵ possess significantly large values in the areas occupied by the iso-surfaces of λ_{3D} (i.e. regions of swirling/rotational motion).

Based on the results discussed above, one might assume that that almost all dissipation occurring in the flow field is from these sheet structures. However, regions of intense dissipation contribute to only a small part of the total dissipation in the flow field. This aspect can be investigated by computing the percentage contribution of intense dissipation to the total dissipation. The cumulative dissipation from points with dissipation up to and greater than a certain threshold and its percentage contribution to the total dissipation in the flow field was computed. Thus

$$CD = \frac{\sum \epsilon(\epsilon > \epsilon_t)}{\sum \epsilon} \tag{4.1}$$

$$UD = \frac{\sum \epsilon(\epsilon < \epsilon_t)}{\sum \epsilon} = 1 - CD, \tag{4.2}$$

where ϵ_t is the threshold on dissipation, CD is the cumulative dissipation from points where ϵ is greater than ϵ_t and UD is the cumulative dissipation from points where ϵ is less than ϵ_t.

Figure 17(*a*) shows the variation of both CD and UD with ϵ_t. The curves indicate that up to 30 % of the total dissipation comes from values lower than the mean dissipation. Conversely, the intense dissipation regions ($\epsilon > 6\bar{\epsilon}$) contribute only about 10 % to the total dissipation. Therefore, the intense dissipation sheets shown in figure 13 contribute only about 10 % to the total dissipation. Figures 17(*b*)–17(*e*) show four sample realizations of dissipation contours in the x_2–x_3 plane. These contour plots are uncorrelated in time. The dissipation values are normalized by the mean dissipation, and the contours shown range from $0.1\bar{\epsilon}$ to $10\bar{\epsilon}$ and follow a logarithmic distribution. The range of contours shown corresponds to capturing

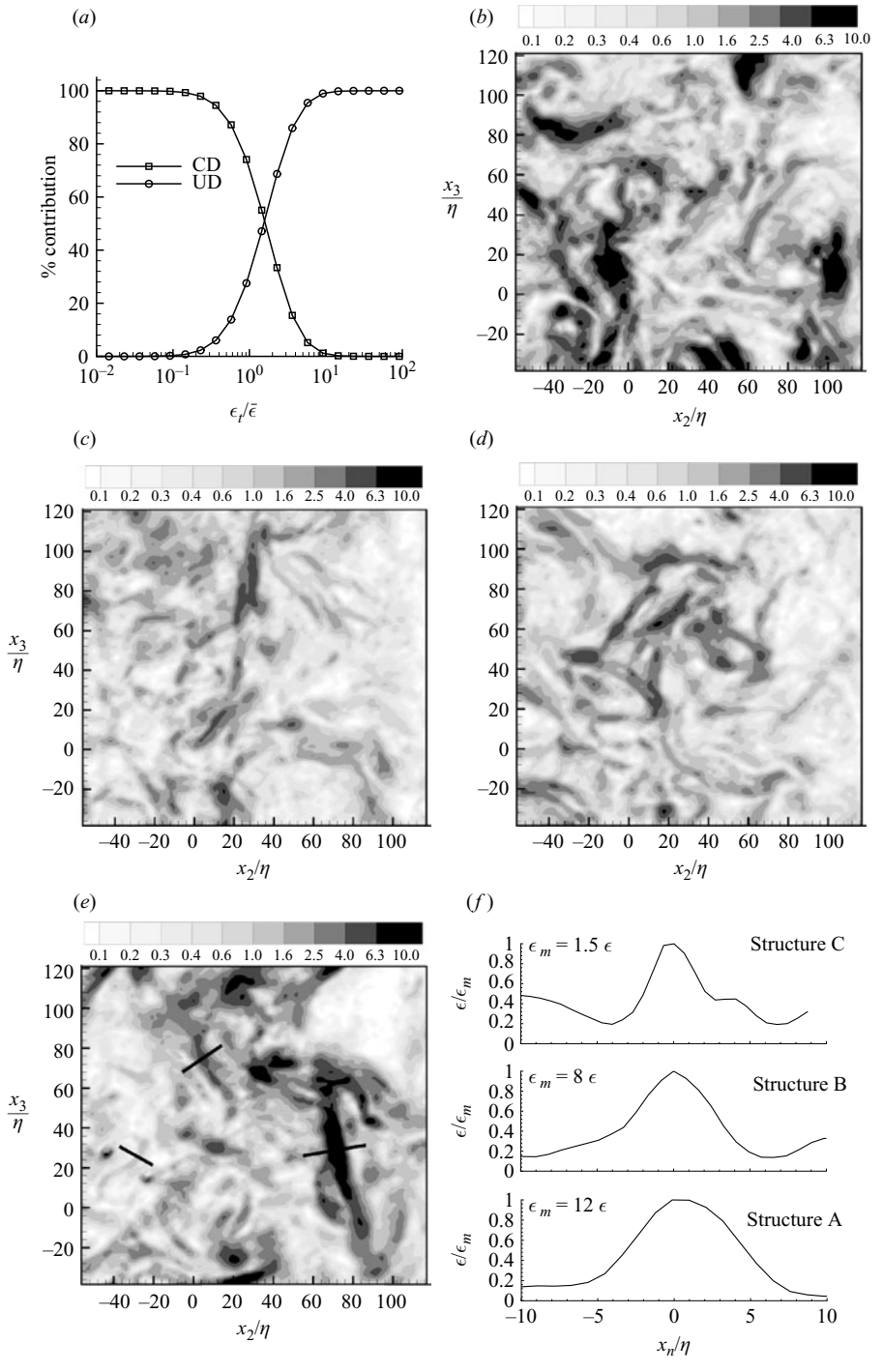

FIGURE 17. (*a*) Percentage contribution to the total dissipation from cumulative dissipation up to and greater than a certain threshold. (*b*)–(*e*) Sample instantaneous planar fields of dissipation in the x_2–x_3 plane. The fields are uncorrelated in time. The dissipation values are normalized by the mean dissipation. The contours shown range from $0.1\overline{\epsilon}$ to $10\overline{\epsilon}$ and the grey-scale values follow a logarithmic scale. (*f*) Profiles of dissipation along lines marked A, B and C in figure 17(*e*).

Quartile	Condition	Percentage contribution
1	$0 < \epsilon < \overline{\epsilon}$	25 %
2	$\overline{\epsilon} < \epsilon < 2\overline{\epsilon}$	25 %
3	$2\overline{\epsilon} < \epsilon < 3\overline{\epsilon}$	25 %
4	$3\overline{\epsilon} < \epsilon < \epsilon_{max}$	25 %

TABLE 4. Regions of dissipation with equal contribution to the total dissipation, as deduced from the cumulative dissipation plots in figure 17(*a*).

99 % of all dissipation in the flow field (as seen in figure 17*a*). These figures indicate that a large amount of area is occupied by regions with dissipation values that are less than the mean dissipation, and these low-dissipation regions seem to exhibit a wide range of scales. Figures 17(*a*)–17(*e*) also indicate that the sheet-like structures of intense dissipation roll off to values less than $\overline{\epsilon}$; however, they tend to maintain the sheet structure. Therefore, these intense dissipation sheets seem to be a part of a larger structure which also possesses a sheet-like structure. This aspect is explored in greater detail later in this section.

Sreenivasan (2004) stated that intense values of kinetic energy dissipation occur over very fine length scales and concluded that the resolution required to capture these intense dissipation regions must be based on the value of instantaneous dissipation and not on the mean dissipation (i.e. resolution $\Delta \approx (\nu^3/\epsilon_t)^{1/4}$, where ϵ_t is a representative value of intense dissipation much greater than the mean dissipation). A plausible interpretation of the above-mentioned resolution requirement is to expect intense dissipative structures to possess smaller length scales (smaller thickness/length) compared to the length scales of structures with lower dissipation values. Figure 17(*f*) shows thickness profiles of three representative dissipation structures marked A, B and C in figure17(*e*). The maximum dissipation within these three structures is $12\overline{\epsilon}$, $6\overline{\epsilon}$ and $1.5\overline{\epsilon}$, respectively. The profiles in figure 17(*f*) indicate that the thickness of structures A, B and C is 12η, 14η and 10η, respectively (following the same definition for thickness used previously in this section). Although structure A is about eight times as intense as structure C and structure B is over four times more intense than structure C, the thicknesses of all three structures are within the same range. This indicates that the magnitude of dissipation does not seem to affect the length scale of a structure. The resolution required to determine the true value of the highest dissipation structures may depend on the instantaneous value of dissipation; however, the profiles in figure 17(*f*) indicate that the structure of a dissipative region can be captured with coarse resolution since the length scale of the these structures do not depend on their magnitude. In fact, a careful viewing of many sample dissipation fields shows that regions of highest dissipation tend to be associated with the largest, not the smallest, sheet-like structures in the flow field. These observations are consistent with the scalar dissipation-based conclusions of Schumacher, Sreenivasan & Yeung (2005) who explored the fine scales of scalar dissipation and found that the very fine scales are unlikely to be related to the most intense dissipation events.

To investigate further the spatial structure of regions of different dissipation magnitude, the total dissipation was divided into four intervals (quartiles) as shown in table 4. Each quartile in the table contributes 25 % of the total dissipation. The characteristics of the structures in each quartile can be visualized as in figures 18(*a*)–18(*d*), which show representative instantaneous plots of the area covered by each quartile (these figures are from the instant shown in figure 17*e*). Note that the

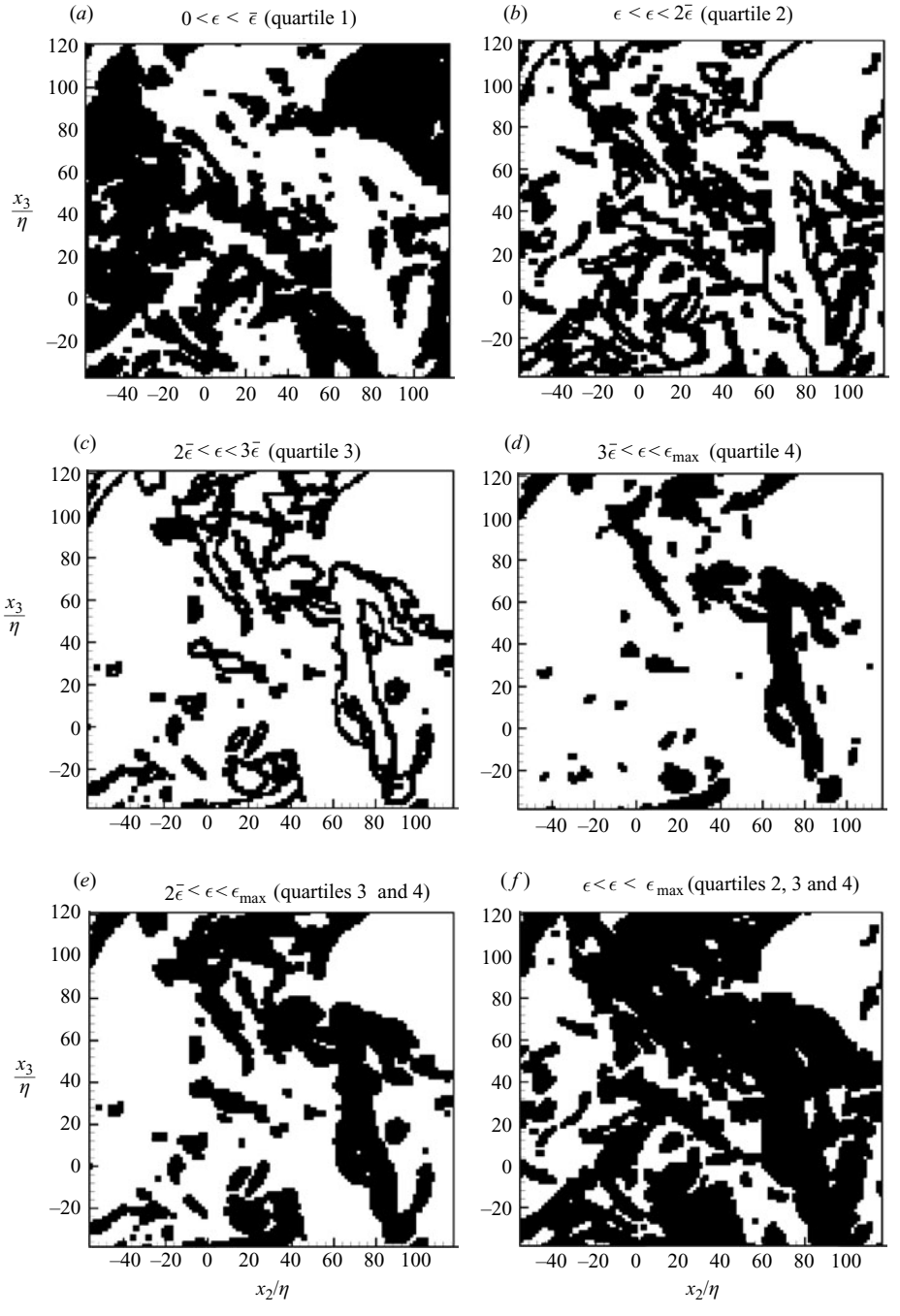

FIGURE 18. Quartiles (marked in black) of equal contribution to the total dissipation at a given instant in the x_2–x_3 plane. The quartiles are split as shown in table 4. (*a*) Quartile 1: $0 < \epsilon < \bar{\epsilon}$. (*b*) Quartile 2: $\bar{\epsilon} < \epsilon < 2\bar{\epsilon}$. (*c*) Quartile 3: $2\bar{\epsilon} < \epsilon < 3\bar{\epsilon}$. (*d*) Quartile 4: $3\bar{\epsilon} < \epsilon < \epsilon_{max}$. (*e*) Quartiles 3 and 4: $2\bar{\epsilon} < \epsilon < \epsilon_{max}$. (*f*) Quartiles 2, 3 and 4: $\bar{\epsilon} < \epsilon < \epsilon_{max}$. The figures are from the instant in figure 17(*e*).

images are binary such that points that lie in a particular quartile are rendered black, and points not in the quartile are white. The bottom 25 % of the total dissipation (quartile 1, figure 18*a*) appears to be in the form of structures that are relatively large. In contrast, the top 25 % of the total dissipation (i.e. quartile 4, figure 18*d*) appears in regions that are in the form of more sheet-like structures. The intermediate 50 % dissipation regions (quartiles 2 and 3) appear to correspond to the outer periphery of the regions of intense dissipation, and these regions appear to form a bridge between quartiles 1 and 4. Figure 18(*g*) shows all points that are either in quartile 3 or 4. The amalgamation of quartiles 3 and 4 does not change the features of the dissipation structure, since the structures still maintain the sheet-like appearance. However, figure 18(*e*) shows that merging quartile 2 with quartiles 3 and 4 seems to considerably alter the structure of the dissipation field. In this case, the dissipation field appears as large blobs with no definite characteristic structure. Therefore, it could be concluded that close to 50 % of the total dissipation are from the extended sheet-like structures. These sheets of intense dissipation occur presumably due to the overlap of the induced strain field of multiple vortex tubes. The remaining 50 % of the total dissipation is from the background, where the induced strain field from the vortex tubes is much weaker.

Observations based on the analysis of quasi-instantaneous volumes of data indicate that intense vorticity possesses extended tube-like structures. The core diameters of these tubes is of order 10η and they extend to lengths of 60–100η in any arbitrary direction. Large-magnitude dissipative regions are in the form of sheets with characteristic thickness of approximately 10η. The size of these sheets (length and width) extends to about 60η. These dissipative regions also contain positive intermediate principal strain, which explains the sheet structure of these regions. The dissipative structures are found in the vicinity of vortex tubes and the length scales of tubes of vorticity and sheets of dissipation are found to be similar, suggesting that these areas of intense dissipation are caused by the interaction between multiple vortex tubes. The presence of multiple intense vortex tubes in the neighbourhood seems to be a necessary condition for the presence of intense dissipation. Examination of several quasi-instantaneous iso-surfaces suggests that extremely intense dissipative structures ($\epsilon > 10\overline{\epsilon}$) are also sheet-like with a size of approximately 30η and are predominantly found in the neighbourhood of a nested group of multiple vortex tubes.

5. Discussion

The sheets of intense dissipation and its surrounding regions (i.e. regions where ϵ is greater than $2\overline{\epsilon}$) contribute close to 50 % of the total dissipation in the flow field. These intense dissipation regions are found in the vicinity of multiple vortex tubes or a cluster of nested vortex tubes. The induced strain fields from these vortex tubes overlap in those regions, resulting in intense kinetic energy dissipation. Figure 19 illustrates the effect of having multiple cores in close proximity. Note that the vortex tubes within a cluster are not necessarily orthogonal. The remaining 50 % of the total dissipation is from regions of low dissipation (i.e. $\epsilon < 2\overline{\epsilon}$). These low-dissipation regions occupy a large fraction of the total area and appear as blobs. The shetch in figure 19 shows that these regions of low dissipation occur in the far field of multiple vortex tubes or in the vicinity of isolated vortex tubes where the strain induced is much weaker.

The observed physical structure of vorticity and dissipation can also be interpreted in terms of the energy and dissipation spectra. Figures 20(*a*) and 20(*b*) show the model

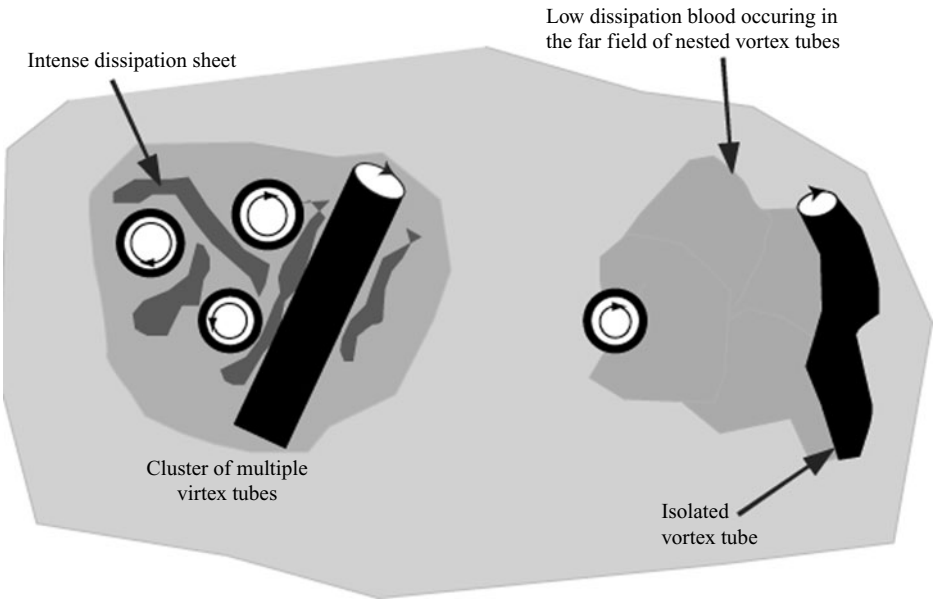

FIGURE 19. Schematic representation of the near- and far-field effects of elongated vortex tubes. Intense dissipation is present in the vicinity of cluster of vortex tubes. Note that the vortex tubes in the cluster are not necessarily orthogonal. Low magnitude dissipation is found in the far field or in the presence of isolated vortex tubes.

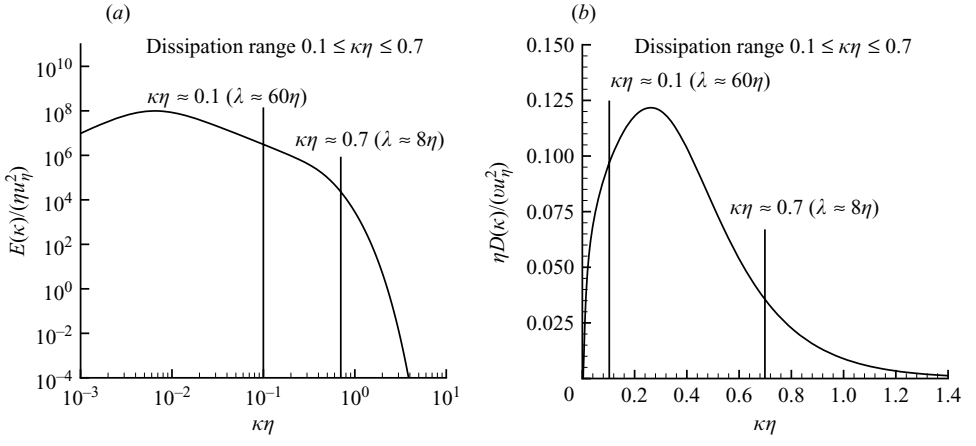

FIGURE 20. (*a*) Three-dimensional model energy spectrum computed using (2.1). (*b*) Dissipation spectrum computed from the model energy spectrum using $D(\kappa) = \kappa^2 E(\kappa)$.

three-dimensional energy spectrum computed from (2.1) and the three-dimensional dissipation spectrum computed as $D(\kappa) = 2\nu\kappa^2 E(\kappa)$. Pope (2000) computed cumulative dissipation to quantify the scales of dissipative motions and concluded that the dissipative range begins at $\kappa\eta \approx 0.1$ (only 10 % of dissipation comes from wavenumbers less than this value) and extends to $\kappa\eta \approx 0.7$ (90 % of dissipation is from wavenumbers below this value). Pope (2000) noted that the dissipative eddies responsible for the bulk of dissipation is in this range.

The lower-bound wavenumber ($\kappa\eta \approx 0.1$) corresponds to a wavelength of approximately 60η ($2\pi\eta/\Lambda \approx 0.1$ results in $\Lambda \approx 20\pi\eta$). Importantly, the three-dimensional instantaneous iso-surfaces in the previous section indicated that the nominal size of dissipation sheets and length of intense vortex tubes is also about 60η. This length scale is also comparable to the Taylor micro-scale that was found to be 65η. This observation is consistent with the model proposed by Tennekes (1968), where the length of the vortex tubes was of order the Taylor scale. It is possible, however, that the agreement between the sheet/tube lengths and the Taylor scale is coincidental, and really just reflects the fact that the range of scales at the current Reynolds number is relatively small. Figure 20(*b*) indicates that the peak in the dissipation spectrum is at $\kappa\eta \approx 0.25$, which corresponds to a length scale of 30η. This length scale is comparable to the size of extremely intense sheets of dissipation. The high-wavenumber bound of the dissipation range $\kappa\eta \approx 0.7$ (wavelength of approximately 8η) physically corresponds to the thickness of intense dissipation sheets and diameter of intense vortex tubes (contrary to the model suggested by Tennekes 1968). It must be noted that the intense dissipation structures contribute only 50 % of the total dissipation. However, all the contributions from the intense structures appear within the above-mentioned wavenumber range, whereas the remaining 50 % of the total dissipation, which is from the background, appear across the entire range of length scales (and therefore the entire wavenumber range).

The high-wavenumber bound for the dissipation range in the spectra indicates a characteristic thickness/diameter for the dissipation sheets/vortex tubes. Similarly, the lower bound for the dissipation range points to the size and the length of dissipative sheets and vortex tubes. This suggests that regions of both intense vorticity and dissipation possess physical length scales that are significantly larger than the theoretical Kolmogorov length scale (Su & Dahm 1996; Buch & Dahm 1998; Mullin & Dahm 2006*b*). Therefore, the Kolmogorov scale is not properly interpreted as the characteristic size of regions of spatially correlated dissipation, since such regions are of order 8 to 10 Kolmogorov scales, or so. Perhaps a better interpretation of the Kolmogorov scale is as a resolution requirement; i.e. it is the scale that must be resolved (within a factor of 2 to 3) in order to resolve the dissipation distributions in the most dissipative structures. In other words, the Kolmogorov scale is the scale that is required to capture (or resolve) the thickness profile of the dissipation sheets or the cores of the vortex tubes. At the Kolmogorov scale, the gradients contribute negligibly to the mean dissipation, but more significantly to the peak dissipation events.

6. Conclusions

Cinematographic stereoscopic PIV experiments were performed to resolve small and intermediatec scales (scale: $\approx 3\eta$–160η) in the far field of an axisymmetric co-flowing jet. Measurements were performed in a plane normal to the axis of the jet. The time-resolved velocity measurements were then converted into a quasi-instantaneous three-dimensional reconstruction of the jet. Taylor's hypothesis was applied to the data along the jet axial direction to reconstruct the axial spatial extent. The availability of quasi-three-dimensional data enabled computation of all nine components of the velocity gradient tensor over the volume, which could be utilized to investigate the structure of dissipation and vorticity.

The (r.m.s.) of the velocity gradients and the three components of vorticity were all found to satisfy the axisymmetric isotropy conditions proposed by George & Hussein (1991) to within 10 %. The mean dissipation value ($\bar{\epsilon}$) was also found to be

consistent with the dissipation estimate computed following the axisymmetric isotropy conditions.

The relationship between the strain-rate field and the vorticity was investigated by calculating the orientation of the principal eigenvectors of the strain-rate tensor with respect to the vorticity vector. The results indicate that the vorticity vector is most likely to be oriented along the intermediate strain and is least likely to be along the largest compressive strain, in agreement with previous studies. Conditional p.d.f.s of normalized intermediate strain indicate that regions of intense vorticity possess a marginal preference for positive values of intermediate strain. Although the conditional mean value of β^* is positive for various thresholds of enstrophy, it remains a constant with increasing threshold, indicating that regions of intense enstrophy do not have a preference for intense positive or negative β^*. Joint p.d.f.s between dissipation and the intermediate principal strain indicate that the regions of intense dissipation tend to occur at locations where the strain field is sheet-forming. The conditional mean value of β^* increases with increasing threshold of dissipation, suggesting that intense dissipation values occur in regions of intense intermediate strain. This observation reinforces the conclusion that dissipation structures are sheet-like due to the presence of two high-magnitude extensive principal strains.

The availability of quasi-instantaneous space–time volumes of data enable visualization of iso-surfaces of strain rate, vorticity and dissipation that can shed light on the structure of intermediate and fine scales of turbulent flow. Investigation of iso-surfaces of swirling strength in a quasi-instantaneous volume reveals that the intense vortex structures are elongated in one direction and appear to be in the form of 'worms'. A cross-sectional view of these 'worms' indicates that these vortex cores have a diameter of approximately 10η, consistent with results from DNS of isotropic turbulence (for example, Siggia 1981; Jimenez *et al.* 1993). The characteristic length of the worms is about 60–100η.

Iso-surfaces of intermediate strain rate and dissipation show that the regions of intense positive intermediate strain and intense dissipative regions are coincident and are in the form of sheets. The dissipation sheets are found to be in the neighbourhood of intense vortex tubes and extremely intense dissipation sheets ($\epsilon > 10\overline{\epsilon}$) appear in the vicinity of multiple nested vortex tubes. Intense dissipation does not occur within a vortex tube but results from the interaction between the nested groups of vortex tubes. Analysis of thickness profiles of the dissipation sheets (in a plane normal to the axis of the sheet) indicates that the thickness varies between 6η and 12η. The largest length scale of these sheets (length or width) extends to 60η. These intense dissipation sheets contribute close to 50 % of the total dissipation in the flow field. The remaining 50 % of the total dissipation is from the background where the instantaneous value of dissipation is close to or less than the mean value of dissipation.

Visualization of quasi-instantaneous data indicates that the intense dissipative structures and vortex tubes possess physical scales that are much larger than the Kolmogorov scale, which is consistent with the findings based on investigation of energy and dissipation spectra. The dissipation range in the dissipation spectrum (i.e. $0.1 < \kappa\eta < 0.7$, the range of wavenumbers that contribute to the bulk of the dissipation) is consistent with length scales of intense vortex tubes and dissipation sheets. The lower bound for the dissipation range ($\kappa\eta \approx 0.1$) corresponds to a length scale of approximately 60η, which is analogous to the length of vortex tubes and dissipation sheets. Similarly, the upper bound of the dissipation range ($\kappa\eta \approx 0.7$, which corresponds to a length scale $\approx 8\eta$) is consistent with the thickness of dissipation sheets and the diameter of the vortex tubes.

The experimental data presented in this study were obtained at the University of Texas at Austin where the first author spent two years as a post-doctoral fellow between November 2004 and December 2006. This work was supported by the US Air Force Office of Scientific Research under grant FA9550-04-1-0387 and the US National Science Foundation under grant CTS-0308589. The authors acknowledge one of the referees for pointing out certain issues with the analysis.

REFERENCES

Antonia, R. A., Kim, J. & Browne, L. W. B. 1991 Some characteristics of small-scale turbulence in a turbulent duct flow. *J. Fluid Mech.* **233**, 369–388.

Antonia, R. A., Satyaprakash, B. R. & Hussain, A. K. M. F. 1980 Measurements of dissipation rate and some other characteristics of turbulent plane and circular jets. *Phys. Fluids* **23**, 695–700.

Antonia, R. A., Satyaprakash, B. R. & Hussain, A. K. M. F. 1982 Statistics of fine-scale velocity in turbulent plane and circular jets. *J. Fluid Mech.* **119**, 55–89.

Ashurst, W. T., Kerstein, A. R., Kerr, R. M. & Gibson, C. H. 1987 Alignment of vorticity and scalar gradient with strain rate in simulated Navier–Stokes turbulence. *Phys. Fluids* **30**, 2343–2353.

Batchelor, G. K. & Townsend, A. A. 1949 The nature of turbulent motion at large wave-numbers. *Proc. R. Soc. Lond.* A **199**, 238–255.

Betchov, R. J. 1956 An inequality concerning the production of vorticity in isotropic turbulence. *J. Fluid Mech.* **1**, 497–504.

Brachet, M. E. 1991 Direct simulation of three-dimensional turbulence in the Taylor–Green vortex. *Fluid Dyn. Res.* **8**, 1–8.

Buch, K. A. & Dahm, W. J. A. 1996 Experimental study of the fine-scale structure of conserved scalar mixing in turbulent shear flows. Part 1. $Sc \ll 1$. *J. Fluid Mech.* **317**, 21–71.

Buch, K. A. & Dahm, W. J. A. 1998 Experimental study of the fine-scale structure of conserved scalar mixing in turbulent shear flows. Part 2. $Sc \approx 1$. *J. Fluid Mech.* **364**, 1–29.

Chakraborty, P., Balachandar, S. & Adrian, R. J. 2005 On the relationships between local vortex identification schemes. *J. Fluid Mech.* **535**, 189–214.

Cucitore, R., Quadrio, M. & Baron, A. 1999 On the effectiveness and limitations of local criteria for the identifcation of a vortex. *Eur. J. Mech.* B/*Fluids* **18**, 261–282.

Douady, S., Couder, Y. & Brachet, M. E. 1991 Direct onservation of the intermittency of intense vorticity filaments in turbulence. *Phys. Rev. Lett.* **67**, 983–986.

Dubief, Y. & Delcayre, F. 2000 On coherent-vortex identification in turbulence. *J. Turbulence* **1**, 1–22.

Frisch, U. 1995 *Turbulence: The Legacy of A. N. Kolmogorov*. Cambridge University Press.

Ganapathisubramani, B., Lakshminarasimhan, K. & Clemens, N. T. 2006 Cinematographic stereoscopic PIV of a turbulent jet: Assessment of accuracy of 3D derived quantities. In *36th AIAA Fluid Dynamics Conference and Exhibit*, Paper # 2006-2806.

Ganapathisubramani, B., Lakshminarasimhan, K. & Clemens, N. T. 2007 Determination of complete velocity gradient tensor using cinematographic stereoscopic particle image velocimetry in the far field of a turbulent jet. *Exps. Fluids* **42**, 923–939.

George, W. K. & Hussein, H. J. 1991 Locally axisymmetric turbulence. *J. Fluid Mech.* **233**, 1–23.

Jeong, J. & Hussain, F. 1995 On the identification of a vortex. *J. Fluid Mech.* **258**, 69–94.

Jimenez, J., Wray, A. A., Saffman, P. G. & Rogallo, R. S. 1993 The structure of intense vorticity in isotropic turbulence. *J. Fluid Mech.* **255**, 65–90.

Kerr, R. M. 1985 Higher-order derivative correlations and the alignment of small-scale structures in isotropic numerical turbulence. *J. Fluid Mech.* **153**, 31–58.

Kida, S. & Ohkitani, K. 1992 Spatiotemporal intermittency and instability of a forced turbulence. *Phys. Fluids* **4**, 1018–1027.

Kolmogorov, A. N. 1962 A refinement of previous hypotheses concerning the local structure of turbulence in viscous incompressible fluid at high Reynolds number. *J. Fluid Mech.* **13**, 82–85.

Kuo, A. Y.-S. & Corrsin, S. 1971 Experiments on the internal intermittency and fine-structure distribution functions in fully turbulent fluid. *J. Fluid Mech.* **50**, 285–320.

Lund, T. S. & Rogers, M. M. 1994 An improved measure of strain state probability in turbulent flows. *Phys. Fluids* **6**, 1838–1847.

Lundgren, T. S. 1982 Strained spiral vortex model for turbulent fine structure. *Phys. Fluids* **25**, 2193–2203.

Melander, M. V. & Hussain, F. 1993 Coupling between a coherent structure and fine-scale turbulence. *Phys. Rev.* E **48**, 2669–2689.

Mi, J. & Nathan, G. J. 2003 The influence of probe resolution on the measurement of a passive scalar and its derivatives. *Exps. Fluids* **34**, 687–696.

Monin, A. S. & Yaglom, A. M. 1975 *Statistical Fluid Mechanics, Vol. 2*. MIT Press, Cambridge, MA.

Mullin, J. A. & Dahm, W. J. A. 2006*a* Dual-plane stereo particle image velocimetry measurements of velocity gradient tensor fields in turbulent shear flow. Part I. Accuracy assessments. *Phys. Fluids* **18**, 1–18.

Mullin, J. A. & Dahm, W. J. A. 2006*b* Dual-plane stereo particle image velocimetry measurements of velocity gradient tensor fields in turbulent shear flow. Part II. Experimental results. *Phys. Fluids* **18**, 1–28.

Pope, S. B. 2000 *Turbulent Flows*. Cambridge University Press.

Pradeep, D. S. & Hussain, F. 2006 Transient growth of perturbations in a vortex column. *J. Fluid Mech.* **550**, 251–288.

Raffel, M., Willert, C. & Kompenhans, J. 1998 *Particle Image Velocimetry*. Springer.

Ruetsch, G. R. & Maxey, M. R. 1991 Small-scale features of vorticity and passive scalar fields in homogeneous isotropic turbulence. *Phys. Fluids* **3**, 1587–1597.

Ruetsch, G. R. & Maxey, M. R. 1992 The evolution of small-scale structures in homogeneous isotropic turbulence. *Phys. Fluids* **4**, 2747–2760.

Saarenrinne, P. & Piirto, M. 2000 Turbulent kinetic energy dissipation rate estimation from PIV vector fields. *Exps. Fluids* **Suppl.**, S300–S307.

Saarenrinne, P., Piirto, M. & Eloranta, H. 2001 Experiences of turbulence measurement with PIV. *Meas. Sci. Technol.* **12**, 1904–1910.

Saddoughi, S. G. & Veeravalli, S. V. 1994 Local isotropy in turbulent boundary layers at high Reynolds number. *J. Fluid Mech.* **268**, 333–372.

Schumacher, J., Sreenivasan, K. R. & Yeung, P. K. 2005 Very fine structures in scalar mixing. *J. Fluid Mech.* **531**, 113–122.

Schwarz, K. W. 1990 Evidence for organized small-scale structure in fully developed turbulence. *Phys. Rev. Lett.* **64**, 415–418.

Siggia, E. D. 1981 Numerical study of small-scale intermittency in three-dimensional turbulence. *J. Fluid Mech.* **107**, 375–406.

Sreenivasan, K. R. 2004 Possible effects of small-scale intermittency in turbulent reacting flows. *Flow, Turulence and Combustion* **72**, 115–131.

Sreenivasan, K. R. & Antonia, R. A. 1997 The phenomenology of small-scale turbulence. *Annu. Rev. Fluid Mech.* **29**, 435–472.

Su, L. K. & Dahm, W. J. A. 1996 Scalar imaging velocimetry measurements of the velocity gradient tensor field in turbulent flows. Part II. Experimental results. *Phys. Fluids* **8**, 507–521.

Tao, B., Katz, J. & Meneveau, C. 1999 Application of HPIV data of turbulent duct flow for turbulence modelling. In *Proc. 3rd ASME/JSME Joint Fluids Engineering Conference*.

Tennekes, H. 1968 Simple model for the small-scale structure of turbulence. *Phys. Fluids* **11**, 669–671.

Tsinober, A., Kit, E. & Dracos, T. 1992 Experimental investigation of the field of velocity gradients in turbulent flows. *J. Fluid Mech.* **242**, 169–192.

Tsinober, A., Shtilman, L. & Vaisburd, H. 1997 A study of properties of vortex stretching and enstrophy generation in numerical and laboratory turbulence. *Fluid Dyn. Res.* **21**, 477–494.

Tsurikov, M. 2003 Experimental investigation of the fine-scale structure in turbulent gas-phase jet flows. PhD thesis, Department of Aerospace Engineering and Engineering Mechanics, The University of Texas at Austin, USA.

Vincent, A. & Meneguzzi, M. 1991 The spatial structure and statistical properties of homogeneous turbulence. *J. Fluid Mech.* **225**, 1–20.

Vincent, A. & Meneguzzi, M. 1994 The dynamics of vorticity tubes in homogeneous turbulence. *J. Fluid Mech.* **258**, 245–254.

Yamamoto, K. & Hosokawa, I. 1988 A decaying isotropic turbulence pursued by the spectral method. *J. Phys. Soc. Japan* **57**, 1532–1535.

Zeff, B. W., Lanterman, D. D., McAllister, R., Roy, R. & E. J. Kostelich, D. P. L. 2003 Measuring intense rotation and dissipation in turbulent flows. *Nature* **421**, 146–149.

Zhou, J., Adrian, R. J., Balachandar, S. & Kendall, T. M. 1999 Mechanisms for generating coherent packets of hairpin vortices in channel flow. *J. Fluid Mech.* **387**, 353–396.